

## Supplementary Materials for **Engineering extrinsic disorder to control protein activity in living cells**

Onur Dagliyan, Miroslaw Tarnawski, Pei-Hsuan Chu, David Shirvanyants,  
Ilme Schlichting, Nikolay V. Dokholyan,\* Klaus M. Hahn\*

\*Corresponding author. Email: khahn@med.unc.edu (K.M.H.); dokh@email.unc.edu (N.V.D.)

Published 16 December 2016, *Science* **354**, 1441 (2016)  
DOI: 10.1126/science.aah3404

### This PDF file includes

Materials and Methods

Figs. S1 to S30

Tables S1 to S3

References

Movie captions S1 to S11

**Other Supplementary Material for this manuscript includes the following:**  
(available at [www.sciencemag.org/content/354/6318/1441/suppl/DC1](http://www.sciencemag.org/content/354/6318/1441/suppl/DC1))

Movies S1 to S11



## Supplementary Materials for **Engineering extrinsic disorder to control protein activity in living cells**

Onur Dagliyan, Miroslaw Tarnawski, Pei-Hsuan Chu, David Shirvanyants, Ilme Schlichting, Nikolay V. Dokholyan<sup>\*</sup>, and Klaus M. Hahn<sup>\*</sup>

correspondence to: khahn@med.unc.edu or dokh@email.unc.edu

### **This PDF file includes:**

Materials and Methods  
Figs. S1 to S30  
Tables S1 to S3  
Captions for Movies S1 to S11  
References

### **Other Supplementary Materials for this manuscript includes the following:**

Movies S1 to S11

## **Materials and Methods**

### DNA construction

The cDNA of the LOV2 domain from *Avena sativa* (oat) Phototropin1 (L404-L547) was used to generate photo-sensitive constructs. Three variants of LOV2 were used: wild-type, dark mutant (C450M or C450A), and lit mutant (I510E/I539E). All point mutations and insertions of LOV2 or uniRapR were performed using QuikChange (Agilent) protocol. Megaprimer for QuikChange were produced using Phusion (New England BioLabs). Insertions sites in target proteins for LOV2 and uniRapR are given in Table S3. To produce fibroblasts that stably express the proteins, DNA constructs were cloned into pBabe-Tet-Off (Clontech) retroviral plasmids that carry either mCherry or mVenus for imaging. For transient expression, constructs were cloned into pmCherry-C1, pmCherry-N1, pmVenus-C1 or pmVenus-N1. Biosensor cDNAs were built based on the design used in our published dual chain FRET sensors (27) with the following modifications: Turquoise/YPet, CyPet/YPet, and Cerulean3/YPet fluorescent protein pairs (31-33) were used to build the Rac1, RhoA, and Cdc42 biosensors, respectively. To produce constant ratios of effector and GTPase expression, ribosome skipping sequences T2A and P2A (34) were inserted between YFP-Effector and CFP-GTPase sequences. In Rac1 sensor variants, an isoleucine-asparagine linker was used at the C-terminus of the PBD domain from p21 protein activated kinase 1 (PAK1), and an alanine residue was used at the N-terminus of dTurquoise. In RhoA biosensor variants, a lysine-leucine linker was used at the C-terminus of YPet, and an alanine-alanine-alanine linker was used at the N-terminus of CyPet. In Cdc42 sensor variants, a glutamic acid-phenylalanine linker was used at the C-terminus of CBD domain from Wiskott Aldrich Syndrome Protein (WASP), and a leucine-glutamine-FLAG-glycine-threonine-glycine tag was at the N-terminus of dTurquoise. GEF-H1 cDNA was a gift from Robert Rottapel (University of Toronto). Rac1(G15A)-GST, RhoA(T17A)-GST, and Cdc42(G15A)-GST in pGEX-4TI bacterial expression plasmids were a gift from Keith Burridge (UNC Chapel Hill). The pProExHTb (Life Technologies) vector encoding for human Cdc42 (Isoform 1, 1-188, C188S) with an N-terminal TEV-cleavable hexahistidine tag was a gift from John Sondek (UNC Chapel Hill). For structural studies, PI-ITSN1 (1230-1580) and PI-Rac1 (1-180, Q61L) constructs were cloned into the bacterial expression vectors pET-24d (EMD Biosciences) and pQE-80L (Qiagen), respectively. PI-ITSN1 contained a short C-terminal hexahistidine (His<sub>6</sub>) tag, whereas PI-Rac1 contained an N-terminal hexahistidine tag followed by a Tobacco etch virus (TEV) protease cleavage site.

### Expression, purification and characterization of proteins used for structural studies

Proteins were expressed in *E. coli* strain BL21 Star (DE3) (Life Technologies). At an optical density at 600 nm of 0.8-1.0, expression was induced with isopropyl β-D-1-thiogalactopyranoside (IPTG). PI-ITSN1 and PI-Rac1 constructs were expressed at 18° C overnight in the dark in the presence of 0.1 mM IPTG, while Cdc42 was expressed at 30° C overnight in the presence of 1.0 mM IPTG. Cells were harvested by centrifugation and stored at -80° C. All subsequent purification steps were done protected from light of less than 550 nm (except for Cdc42) at 4° C. The cell pellets were resuspended in buffer A (50 mM NaH<sub>2</sub>PO<sub>4</sub> pH 8.0, 300 mM NaCl, 10 mM imidazole, 10% (v/v) glycerol), Complete EDTA-free protease inhibitors (Roche), 5 mM DTE, 1 mg/ml lysozyme and 10 µg/ml DNaseI. The cells were lysed using a microfluidizer (Microfluidics) operated at a

pressure of 0.7 MPa and the lysates were clarified by centrifugation at 47,800g for 1 hour at 4° C. The cleared supernatants were loaded onto a HisTrap FF (GE Healthcare) column pre-equilibrated with buffer A. The column was washed with buffer A and the protein was eluted in buffer A with 500 mM imidazole. Fractions containing PI-ITSN1 were incubated with excess flavin (FMN) and dialyzed overnight against buffer B (25 mM Tris-HCl pH 8.5, 5 mM MgCl<sub>2</sub>, 3 mM DTE, 5% (v/v) glycerol). After dialysis, the samples were concentrated using Amicon (Millipore) centrifugal units and loaded onto a MonoQ (GE Healthcare) column pre-equilibrated with buffer B. The column was washed with buffer B and the protein was subsequently eluted using linear gradient of 0-500 mM NaCl in the same buffer. Fractions containing PI-ITSN1 were again concentrated and further purified by gel filtration on a Superdex 200 column (GE Healthcare) equilibrated with buffer C (25 mM Tris-HCl pH 8.5, 50 mM NaCl, 5 mM MgCl<sub>2</sub>, 3 mM DTE, 5% (v/v) glycerol). The eluted protein was finally concentrated, aliquoted, frozen in liquid nitrogen and stored at -80° C. After elution from the HisTrap FF column, PI-Rac1 was incubated with excess FMN and GTP, dialyzed overnight against buffer B with TEV protease using a 1:20 molar ratio of TEV:substrate. For PI-Rac1 purification, the pH of both buffer B and buffer C was adjusted to pH 8.0. The dialyzed sample was loaded onto a Ni-NTA column (Qiagen) to remove cleaved His<sub>6</sub>-tag and His<sub>6</sub>-TEV. The flow-through was concentrated and used for further purification steps. Ion exchange and gel filtration chromatography of PI-Rac1 were performed as described above for PI-ITSN1. For purification of human Cdc42, the lysis buffer was additionally supplemented with 200 μM GDP. Cdc42-containing fractions eluted from the HisTrap FF column were incubated with excess GDP and dialyzed overnight against buffer D (25 mM Tris-HCl pH 8.0, 100 mM NaCl, 3 mM DTE, 20 μM GDP, 5% (v/v) glycerol) with TEV protease using a 1:20 molar ratio of TEV:substrate. The dialyzed sample was loaded onto the Ni-NTA column and the flow-through was concentrated and subjected to gel filtration chromatography on a Superdex 75 (GE Healthcare) column equilibrated with buffer D. The eluted protein was concentrated, aliquoted, frozen in liquid nitrogen and stored at -80° C.

### Protein crystallization

Crystallization was performed at 20° C in the dark using the vapor-diffusion method. Crystal handling was done under orange light with a 2 mm thick OG570 filter (Schott, Germany) shielding the microscope bulb to avoid photoactivation. Crystals of PI-ITSN1(WT) and PI-ITSN1(C450M) with a plate-like morphology were grown by mixing equal volumes of protein solution (29 mg/ml for the wild type protein and 19 mg/ml for C450M mutant) and a reservoir solution containing 0.1 M HEPES pH 7.5, 9% (w/v) PEG 8000 and 9% (v/v) ethylene glycol. The crystals were briefly washed in cryoprotectant solution consisting of the reservoir solution with ethylene glycol added to a final concentration of 20% (v/v), prior to flash-cooling in liquid nitrogen. PI-Rac1(C450A) crystals were obtained by mixing equal volumes of protein solution at 18 mg/ml and precipitant solution containing 0.2 M calcium acetate and 26% (w/v) PEG 3350. Very thin and small plate-shaped crystals of PI-Rac1 grew in clusters. Nevertheless, single plates could be isolated and were briefly washed in cryoprotectant solution consisting of the reservoir solution supplemented with 20% (v/v) glycerol before flash-cooling in liquid nitrogen. The complex of PI-ITSN1(WT) and the Cdc42 was formed by mixing both components in a 1:1 stoichiometry and incubating it with 10 mM

EDTA. Rod-shaped crystals were obtained by mixing equal volumes of preformed complex solution at a concentration of 19 mg/ml and reservoir solution containing 0.1 M MES, 20% (w/v) PEG 6000, final pH 6.0. Before flash-cooling the crystals in liquid nitrogen they were briefly washed in cryoprotectant solution composed of the reservoir solution supplemented with 25% (v/v) ethylene glycol.

#### X-ray diffraction data collection and structure determination

Single crystal X-ray diffraction data were collected at 100 K on the X10SA beamline at the SLS (PSI, Villigen, Switzerland). All data were processed with XDS (35). The structures were determined by molecular replacement using Phaser (36) and individual domain coordinates from pdb entries 2wkq and 1ki1 as a search models. The final models were optimized in iterative cycles of manual rebuilding using Coot (37) and refinement using phenix.refine (38). For PI-ITSN1(WT), PI-ITSN1(C450M) and PI-ITSN1(WT):Cdc42 non-crystallographic symmetry (NCS) restraints were included during refinement. The following TLS groups were used for PI-ITSN1(WT/C450M) (chains A and B: 1231-1505, 1506-1723), PI-ITSN1(WT):Cdc42 (chains A and C: 3-178; chains B and D: 1231-1308, 1309-1451, 1452-1582, 1583-1722/3) and PI-Rac1(C450A) (chain A: 3-36, 37-61, 62-195, 196-327) in the final refinement cycles. Data collection and refinement statistics are summarized in Tables S1 and S2. Model quality was validated as implemented in PHENIX. Atomic coordinates and structure factors have been deposited in the Protein Data Bank under accession codes: 5HZJ (PI-ITSN1-WT), 5HZI (PI-ITSN1-C450M), 5HZK (PI-ITSN1-WT:Cdc42), 5HZH (PI-Rac1-C450A).

#### Small angle X-ray scattering

Solution scattering experiments were performed at the cSAXS X12SA beamline at the SLS (PSI, Villigen, Switzerland). A series of protein concentrations ranging from 1.25 to 10 mg/ml of PI-ITSN1(C450M) or PI-ITSN1(C450M):Cdc42 were measured in buffer containing 25 mM Tris-HCl, 100 mM NaCl, 3 mM DTE, 5% (v/v) glycerol. The samples were mounted in 1 mm diameter quartz capillaries under protective light conditions and kept at 10° C during the experiment. Data acquisition was performed using 11.2 keV photons and a beam size of 200-300 μm. 200 measurements of 0.5 s each were recorded at 20 positions along the length of the capillary. Scattered X-rays were recorded with a Pilatus 2M detector placed at a distance of 2154 mm from the sample. Data were collected from the buffer alone and from the buffered protein solutions in the dark. All the data were azimuthally integrated and averaged. For SAXS data analysis, the buffer signal was subtracted from that of the protein solution. The scattering data were evaluated with GNOM (39). Three-dimensional shape reconstruction was performed using DAMMIF (40) and  $q$  range of 0-0.313 Å<sup>-1</sup>, assuming *P1* symmetry and 20 independent models were generated. DAMAVER (41) was used to align independent reconstructions and construct an averaged model. CRYSTAL (42) was used to fit the theoretical scattering calculated from the crystal structure coordinates to the solution scattering data.

#### Hydrogen-deuterium exchange with mass spectrometry

To address the effect of illumination on PI-ITSN1(WT), two deuterium labeling experiments, under dark (d) and blue-light (l) conditions, were performed. Protein

samples were prepared under protective light conditions at a final concentration of 200  $\mu$ M in buffer C. Protein aliquots of 2  $\mu$ l were equilibrated at 20° C under dark or blue-light conditions for 1 min before initiating the labeling reaction. Samples were illuminated using a royal blue (455 nm) LED lamp (Thorlabs) providing a light intensity of 2 mW/cm<sup>2</sup> at the sample position and these conditions were maintained throughout the labeling procedure. Each reaction was performed in triplicate. The labeling reaction was started by addition of 38  $\mu$ l deuteration buffer C<sub>D</sub> (corresponding to buffer C, but prepared with D<sub>2</sub>O and glycer-d<sub>3</sub>-ol and including a D<sub>2</sub>O correction for pD 8.5 at 20° C) and 5  $\mu$ l aliquots were removed after 10 sec, 45 sec, 3 min, 15 min and 60 min.

Deuterium incorporation was terminated by quenching the samples in 55  $\mu$ l of ice-cold 200 mM NH<sub>4</sub>/formic acid buffer (pH 2.5). 55  $\mu$ l of the quenched sample were analyzed using a cooled HPLC setup, as described previously (43). Briefly, deuterated samples were digested on a Poroszyme immobilized pepsin column (Life Technologies) kept at 10° C. The resulting peptic fragments were desalted on a 2 cm Discovery Bio C18 guard column (Sigma) and separated on a XR ODS (75 mm · 3 mm, 2.2  $\mu$ m particle) reverse phase column (Shimadzu) using an acetonitrile gradient (15-50% over 7 min.) in the presence of 0.6% formic acid. Eluting peptides were injected into a maXis electrospray ionization-ultra high resolution-time-of-flight mass spectrometer (Bruker) to measure the extent of deuteration. Deuterium incorporation was analyzed and quantified using the highly automated Hexicon 2 software package (43).

#### Cell lines, transient transfection, retroviral and lentiviral transduction

Mouse embryonic fibroblasts (MEF) stably expressing tetracycline binding element were obtained from Clontech. Mouse embryonic SYF cells were obtained from the ATCC. Transient transfections for live cell imaging were performed using Fugene 6 transfection reagent (Promega) under the guidelines of the manufacturer. Transient transfections for high-content live cell FRET imaging were performed using Plus and Lipofectamine reagents (Thermo Fisher Scientific) under the guidelines of the manufacturer. Lentiviral shRNA for Rac1 (TRCN0000310901) was obtained from Sigma. To stably knock down Rac1 in MEFs, HEK293 human cells were transfected with pLKO-puro lentiviral vector carrying the shRNA with packing and envelope plasmids psPAX2 and pCMV-VSVG using Plus and Lipofectamine reagents under the guidelines of the manufacturer. Retravirus production was also conducted similarly by transfecting HEK293 cells with pBabe-puro or pBabe-hygro construct and retroviral packaging plasmid pCL-Eco. The next day, the medium was replaced with fresh medium and cells were incubated at 37° C for virus production. After 24-48 hours, viruses were collected from the cell media to infect MEF cells treated with polybrene. After 24-48 hours, cells were selected using an antibiotic (puromycin or hygromycin). For PI-Src(WT) experiments, tetracycline binding element were not expressed in SYF cells to obtain low expression (similar to endogenous Src expression levels), enabling simultaneous imaging of focal adhesions and cellular edge using wide-field fluorescence microscopy.

#### High-content live cell FRET imaging

High-content live cell FRET imaging was performed as described previously (44). Briefly, HEK293T cells were seeded on 96-well plates, and cells were transfected with GTPase FRET biosensors (CFP/YFP pair), GEFs or controls using Lipofectamine and

Plus reagents (Invitrogen) as suggested by the manufacturer. Assays were performed 24 hours after transfection. Dose response curves were generated to evaluate the effect of each construct at different expression levels. To test GTPase-LOV2 fusions, biosensors were titrated in the presence of saturating amounts of GEF. To test GEF-LOV2 fusions, the fusions were titrated in the presence of saturating amounts of biosensor. Because the spectrum of wild type LOV2 overlaps with the spectrum of CFP, light-insensitive dark (C450A) and lit (I510E/I539E) mutants of LOV2 were used. An automated microscope (Olympus IX-81 with automated stage, filter wheels and X/Y/Z stage with autofocus) and Metamorph software (44) was used to image each well at CFP, YFP, FRET, and sometimes mCherry wavelengths. A custom-written MATLAB script for image analysis was used to calculate the sum of pixel intensities at each channel, background subtractions, bleed-through corrections, and normalization of FRET to donor ratios for each plate.

#### Fluorometer assays

Fluorometer assays were performed as described previously (45). Briefly, HEK293T cells were seeded on 6-well plates, and cells were transfected with biosensors, GEFs or controls using the Lipofectamine and Plus reagent (Invitrogen) as suggested by the manufacturer. Assays were performed 24 hours after the transfection. Cell suspensions were analyzed using a Fluorolog SPEX 168 fluorometer. Because the spectrum of wild type LOV2 overlaps with the CFP's spectrum, dark (C450A) and lit mutant (I510E/I539E) of LOV2 were used. Samples were excited at 433 nm and emission was collected from 450 to 600 nm. To normalize for biosensor concentration, YFP was directly excited at 505 nm and its emission at 525 nm was measured. All spectra shown were normalized to equal CFP peak value.

#### Single cell live imaging

Cells were plated on coverslips coated with 5 µg/mL of fibronectin (Sigma) and incubated in DMEM growth medium supplemented with 10% (vol/vol) FBS at 37°C. To start expression in Tet-Off cells, doxycycline was removed from the medium 24 hours before imaging. HeLa cells were transfected with Fugene. L15 imaging medium (Invitrogen) supplemented with 2% (vol/vol) FBS was used for imaging. An open heated chamber (Warner Instruments) was used during live cell imaging, which was performed with an Olympus IX-81 microscope equipped with an UPlanFLN 40x objective (Pil, N.A 1.30). Metamorph software (Molecular Devices) was used to control the microscope and acquire images at each time point. YFP and mCherry images were acquired using a 100 Watt mercury arc lamp with a 3% ND filter and a 510–520 nm or 565–595 nm band-pass filter respectively, for 300 ms. For blue light illumination, a 1% ND filter and a 426–446 nm band-pass filter were used with a 100 Watt mercury arc lamp ( $\sim 1\text{nW}/\mu\text{m}^2$  of power density at  $\lambda=488\text{ nm}$ , measured at the specimen plane). Photo-activation and photo-inhibition on the microscope was carried out using a pulse protocol, alternating 5 s light with 5 s dark. Optogenetic imaging was performed at 10 second intervals, whereas cells with uniRapR constructs were imaged at 1 min time intervals.

#### Cell migration assay

Cell migration assays were performed as described previously (46). SYF cells

stably expressing Src derivatives were plated on fibronectin-coated 96-well dishes for 12–18 h in darkness. A vertical scratch was made in each confluent monolayer using a p10 pipet tip. Cell debris was removed by washing the cells with PBS once and replacing with fresh medium. Cells were then returned to the tissue culture incubator with or without light treatment for 7 hours. Images were acquired using phase contrast microscopy with an UPlan FL N Ph1 10X/0.3NA objective. The distances between the wound edges were analyzed using MetaMorph software. Migration rates were obtained from the wound width at 0h and 7h and expressed as migration distance over time ( $\mu\text{m}/\text{min}$ ). For each sample we took four images along the scratch, and 5 readings of gap distance were measured from each of the images. Each experiment was repeated four times for each cell type. As a result, each Src derivative generated 80 readings for gap distance and was plotted as a box plot.

#### Image processing

Cells were masked using the *MovThresh* (47, 48) MATLAB module, which determines an intensity threshold for each time frame. The *Proactive* (47, 48) MATLAB module was used to quantify protrusive and retractive activity. The ImageJ plugin ADAPT (49) was used to analyze cell roundness. Metamorph software (Molecular Devices) was used for background subtraction, and a custom MATLAB script was used for photo-bleaching corrections (50). For experiments shown in Fig. 4, focal adhesions were identified and quantified using the focal adhesion analysis server (FAAS) (<http://gomezlab.bme.unc.edu/tools>) (51, 52). The average adhesion signal outside of the focal adhesions (mostly in perinuclear region) was excluded using Metamorph. The threshold in the server to detect focal adhesions was set to 2. We manually excluded non-focal adhesion signal detected by FAAS. As a result, a total of 245260 data points out of 281225, from 16 cells, were used to generate the plot in Fig. 4.

#### Computational identification of insertion loops

Surface exposure was determined by calculating solvent accessible area (SAA) using Stride (53). Residues that have SAA values higher than  $40 \text{ \AA}^2$  were considered surface-exposed. The same program was also used to automatically determine secondary structures in crystal structures. Domain sequences from multiple species were obtained from Pfam (54). To calculate sequence conservation, we used MISTIC (55) which provides Kullback-Leibler (KL) conservation to calculate the sequence conservation as

$$KL_i = \sum_{i=1}^N \ln \frac{P(i)}{Q(i)}$$

where  $P(i)$  is the frequency of apparition of residue  $i$  in that position and  $Q(i)$  is the background frequency of the residue in nature, obtained from the Uniprot database. The residues that have KL values lower than 2 were considered as non-conserved. Homology models of Vav2 and GEF-H1 were built using I-Tasser (56) using the crystal structures Vav1 (pdb id: 3ky9), and PDZ RhoGEF (pdb id: 3t06), respectively. Loop distances of all proteins from the Protein Data Bank were obtained from ArchDB server (57). Contact maps were built by using the crystal structures or homology models, and two residues were assumed in contact if the distance between their  $\alpha$ -carbons was less than  $7 \text{ \AA}$ . Residue contacts extending perpendicular to the diagonal line represent two interacting

structural units often connected by a tight loop. If this set of contacts reached to the active site (shown as green bands in the maps), the loop was accepted as a mechanically coupled loop.

### Modeling and simulations

Crystal structures and homology models were modeled using the Medusa all-atom system (24). A repulsive potential was applied to J $\alpha$  helix of LOV2 to mimic light-induced unfolding of J $\alpha$ . Structural models were energetically minimized using short discreet molecular dynamics simulations (58, 59) at high temperature (0.7 kcal/mol•k<sub>B</sub>) and high heat exchange coefficient of 10, with a harmonic potential constant of 1 kcal/mol•Å<sup>2</sup>. Packing was performed at low temperature (0.3 kcal/mol•k<sub>B</sub>) with a heat exchange coefficient of 1. Debye-Hückel approximation was used to model screened charge-charge interactions. Debye length was assigned as 10 Å by assuming a monovalent electrolyte concentration of 0.1 mM. Continuous electrostatic interaction potential was discretized with an interaction range of 30 Å, where the screened potential approached zero. Relative permittivity of water was assigned as 80. The simulation time for each trajectory was 50 ns. A simulation of each system at each temperature included ten independent trajectories. Correlative motion maps that represent dynamic coupling were built by computing correlation coefficients of motions between all residues (60). To characterize the conformational changes, average pairwise distances between the  $\alpha$ -carbon atoms were calculated.

### Antibodies

Antibodies were from the following sources: Myc (Millipore), GFP-JL8 (Clontech), phospho-Paxillin-Y31 (Invitrogen), p130Cas (Cell Signaling), Cortactin (Cell Signaling), FAK (a gift from Michael Schaller), Paxillin (a gift from Michael Schaller), phospho-EGFR-Y1068 (Cell Signaling), EGFR (Cell Signaling), phospho-MEK-S217/221 (Cell Signaling), MEK (Cell Signaling), phospho-Cofilin-S3 (Cell Signaling), Cofilin (Cell Signaling), Src (Cell Signaling), Vinculin (Cell Signaling), GST (Cell Signaling), and mCherry (Clontech).

### Immunoprecipitation and kinase assays

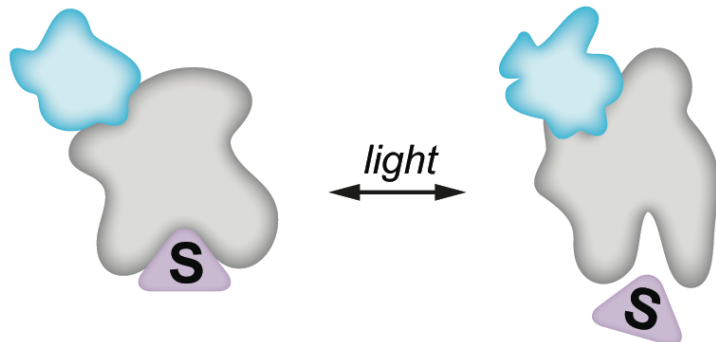
*In vitro* kinase assays were performed as described previously (14). Briefly, myc-tagged Src kinases variants were expressed in 293 LinXE cells for 24 h in the dark. Cells were washed with cold PBS and lysed with lysis buffer (20 mM HEPES-KOH, pH 7.8, 50 mM KCl, 100 mM NaCl, 1mM EGTA, 1% NP40, 1mM NaF and 0.1 mM Na<sub>3</sub>VO<sub>4</sub>). Cell lysates were then clarified by centrifugation at 3,000 x g for 10 min at 4° C. The kinases were then purified from cleared lysates by incubating anti-myc antibody coated IgG-linked agarose beads with cell lysate for 2 hours at 4 °C. The beads were washed two times with wash buffer (20 mM HEPES-KOH, pH 7.8, 50 mM KCl, 100 mM NaCl, 1mM EGTA, 1% NP40) and two times with kinase reaction buffer (25 mM HEPES, pH 7.5, 5 mM MgCl<sub>2</sub>, 5 mM MnCl<sub>2</sub>, 0.5 mM EGTA). The immunoprecipitates were suspended in kinase reaction buffer. All procedures were carried out in a room illuminated with red light or samples were covered with aluminum foil. We used blue light LED panel to illuminate the specimens (~ 0.02 nW/μm<sup>2</sup> power density at λ=445 nm). We used a pulsed protocol, alternating 10 s light with 10 s dark. Precipitates were aliquotted into 1.5-ml

eppendorf tubes and placed on ice under illumination. Samples to be kept in the dark were covered with aluminum foil. Kinase assays were carried out at room temperature under ambient light in the presence of ATP. A purified N-terminal fragment of paxillin (61) was used as a substrate for 5 minutes. The reactions were stopped by adding 2X Laemmli protein sample buffer. The reaction mixture was then analyzed by Western blot using an anti-GFP antibody to measure the levels of kinase protein and an anti-phospho-Y31-Paxillin antibody to measure the levels of phosphorylated substrate. To assay the tyrosine kinase activity of Src variants, transiently transfected 293 LinXE cells or SYF stable cell lines were washed with cold PBS, lysed in 300 µl of sample buffer, and blotted with anti-pTyr (4G10) antibody (Millipore). Due to the low abundance of p130Cas, FAK, and cortactin, we immunoprecipitated these endogenous substrates and monitored their phosphorylation with a phospho-tyrosine antibody. Paxillin, EGFR, MEK, cofilin, Src, and vinculin (loading control) were examined directly in cell lysates.

#### Biochemical GEF activity assays

Pull-down to quantify the amount of active GEF was performed as described previously (62). Briefly, *E. coli* BL21 was transformed with GST-GTPase (Rac1(G15A)-GST, RhoA(T17A)-GST, and Cdc42(G15A)-GST) plasmid and grown overnight to full density (O.D > 1.0), induced with 100 µM of IPTG, and then incubated at room temperature overnight. Bacteria were lysed with lysis buffer (20 mM HEPES pH 7.5; 150 mM NaCl; 5 mM MgCl<sub>2</sub>; 1% Triton X-100; 1 mM DTT with protease inhibitors), sonicated, and clean lysate was equilibrated with glutathione sepharose slurry at 4° C for an hour. After washing with HBS (20 mM HEPES, pH 7.5; 150 mM NaCl), protein concentration was estimated using Coomassie Plus protein reagent (Pierce). Proteins attached to beads can be stored at -80 °C with 0.5 volumes of glycerol. After obtaining GST-GTPase proteins, 293T cells transfected with GEF constructs were lysed, and cleaved lysates were incubated with beads/GST/GTPase for 60 minutes at 4°C. Blue light exposure was performed under the same conditions used for kinase assays. Beads were washed with lysis buffer and the presence of active GEF, total Rac1 and Vav2 input from 293T cells were examined with Western blotting. An mCherry antibody (Clontech) was used to detect mCherry-GEFs in lysates and immunoprecipitated samples.

## Opto-allosteric inhibition



## Chemo-allosteric activation

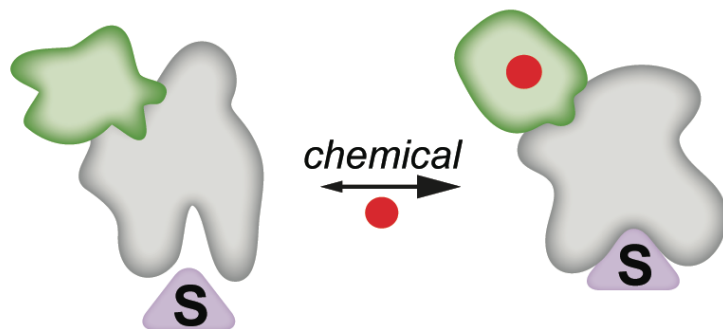


**Fig. S1. Opto-allosteric and chemo-allosteric control of protein activity.** (Top) Light-induced conformational change of the LOV2 domain (blue) inserted into the host protein (gray) leads to distortion of the host protein. LOV2 returns to the dark state with  $t_{1/2} = 18.5$  s in living cells at 37° C (26). The recovery kinetics of LOV2 can be tuned by introducing LOV2 mutations (26). For example, I427T ( $t_{1/2}=1.7$  s) and V416L ( $t_{1/2}=496$  s) mutants can be used to produce fast and slow recovery, respectively. Slow recovery enables maintenance of the lit state with a pulse of light every few minutes. (Bottom) addition of rapamycin (or its non-immunosuppressive analogs) reduces the distortion introduced by the the uniRapR domain (green), resulting in re-activation of the host protein. S denotes substrate or protein target.

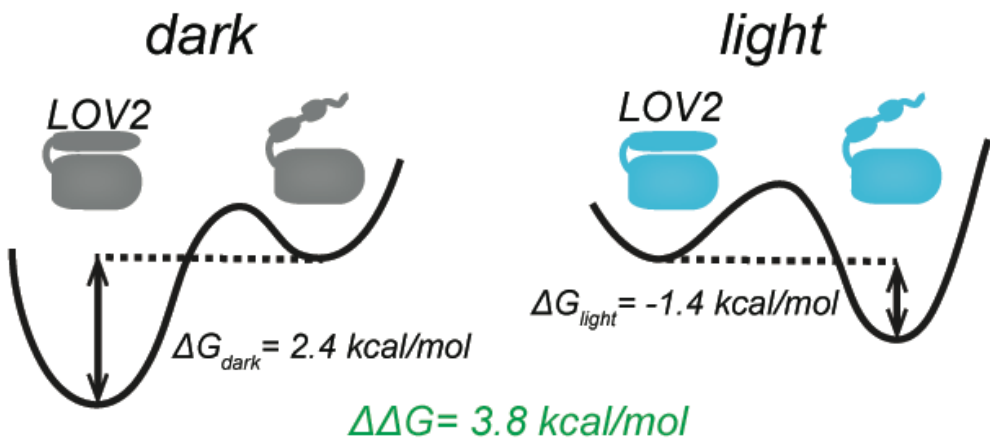


**Fig. S2. Light-induced equilibrium shift of LOV2.** The estimated free energy differences between the ground and excited states of the LOV2-J $\alpha$  complex are 2.4 kcal/mol and -1.4 kcal/mol in the dark and light, respectively. Upon light absorption, a total of 3.8 kcal/mol of energy becomes available for transmission from LOV2 to the attached protein (adapted from (63)).

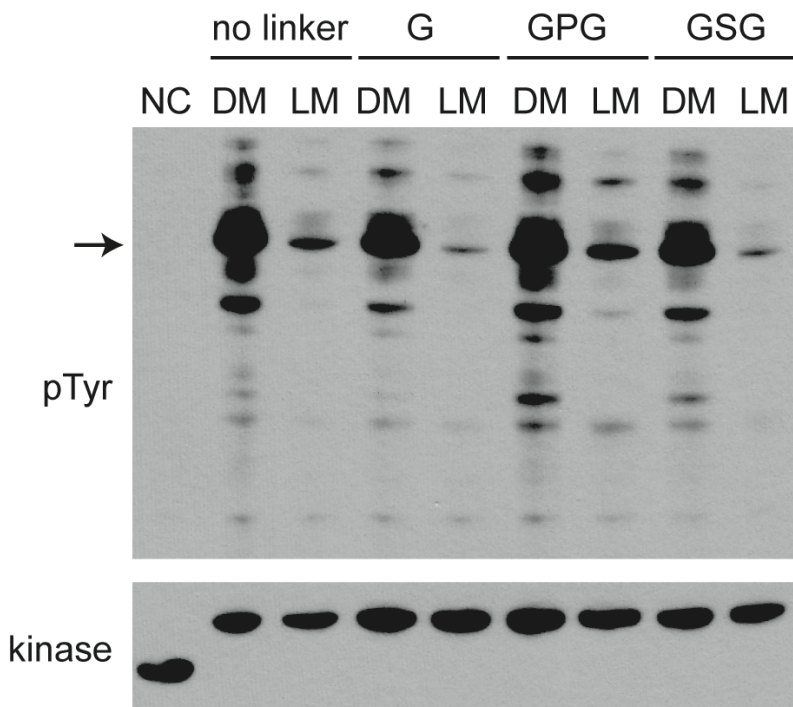


**Fig. S3. Effect of linkers on LOV2-Src fusions.** DM and LM denote dark state and lit state mutants. Kinase activity was determined by Western blotting using an anti-pTyr antibody. Protein levels of fluorescently tagged kinases were detected using anti-GFP antibody. Linkers are attached between each terminus of LOV2 and Src kinase. NC denotes negative control (kinase-dead Src). G, P, and S denotes glycine, proline, and serine, respectively. The arrow indicates auto-phosphorylation of exogenous PI-Src, which is not present in the NC sample.

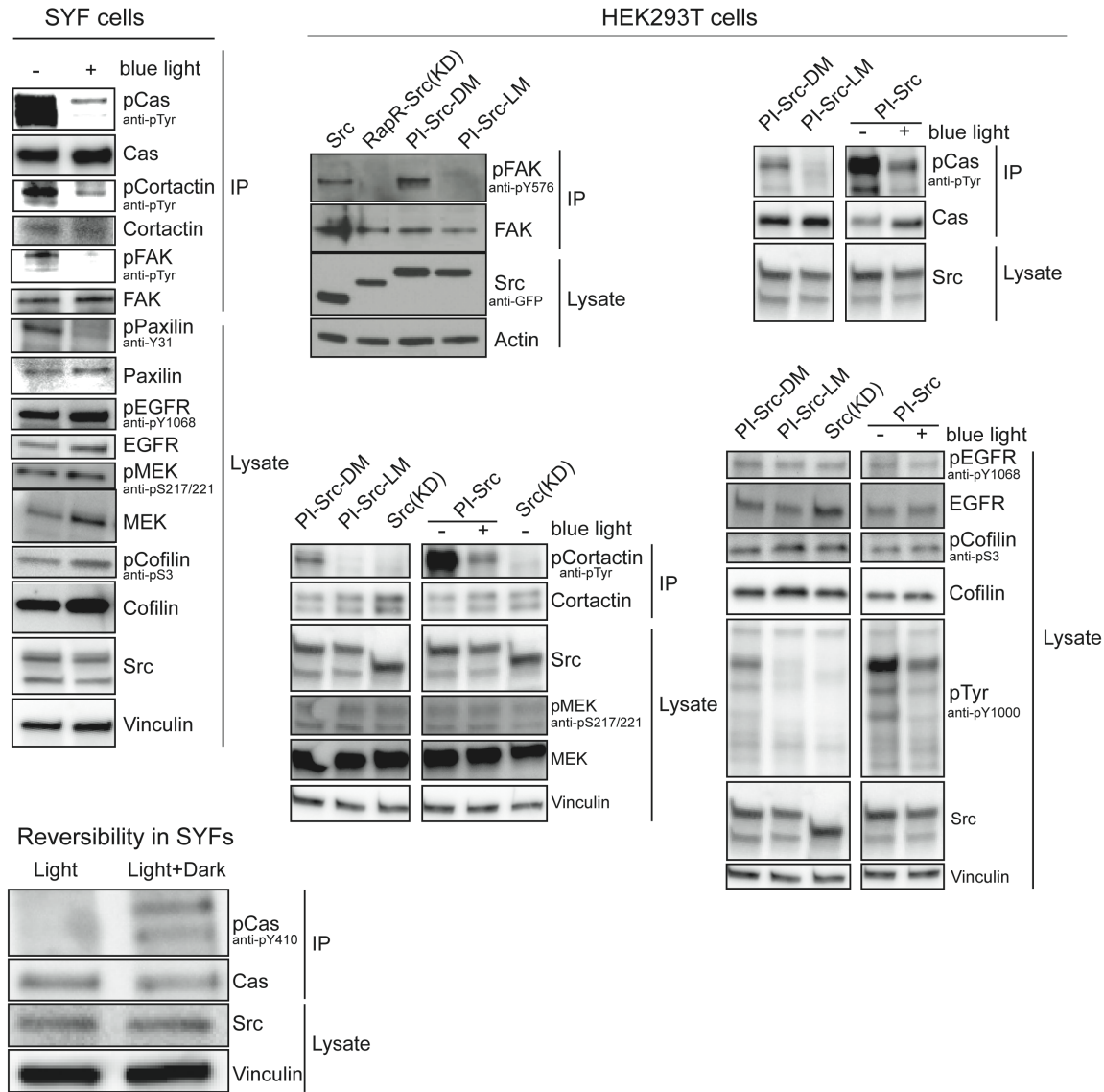


**Fig. S4. Effect of PI-Src photo-inhibition on the phosphorylation of endogenous substrates.** We examined the phosphorylation of Src substrates (p130Cas, focal adhesion kinase (FAK), cortactin and paxillin) and non-substrates (EGFR, MEK, and cofilin) in SYF and HEK293T cells. SYF and HEK293T cells that express PI-Src with wild type LOV2 were irradiated for an hour before cell lysis. To test the reversibility of PI-Src, SYF cells were irradiated (1h), and then incubated in the dark (1h) before cell lysis. Due to the low abundance of p130Cas, FAK, and cortactin, we immunoprecipitated endogenous substrates and monitored their phosphorylation with a phospho-tyrosine antibody. Paxillin, EGFR, MEK, cofilin, Src, and vinculin (loading control) were examined directly in cell lysates. IP denotes immunoprecipitated samples. RapR-Src(KD) is a negative control (kinase-dead Src). DM and LM denote dark and lit mutants.

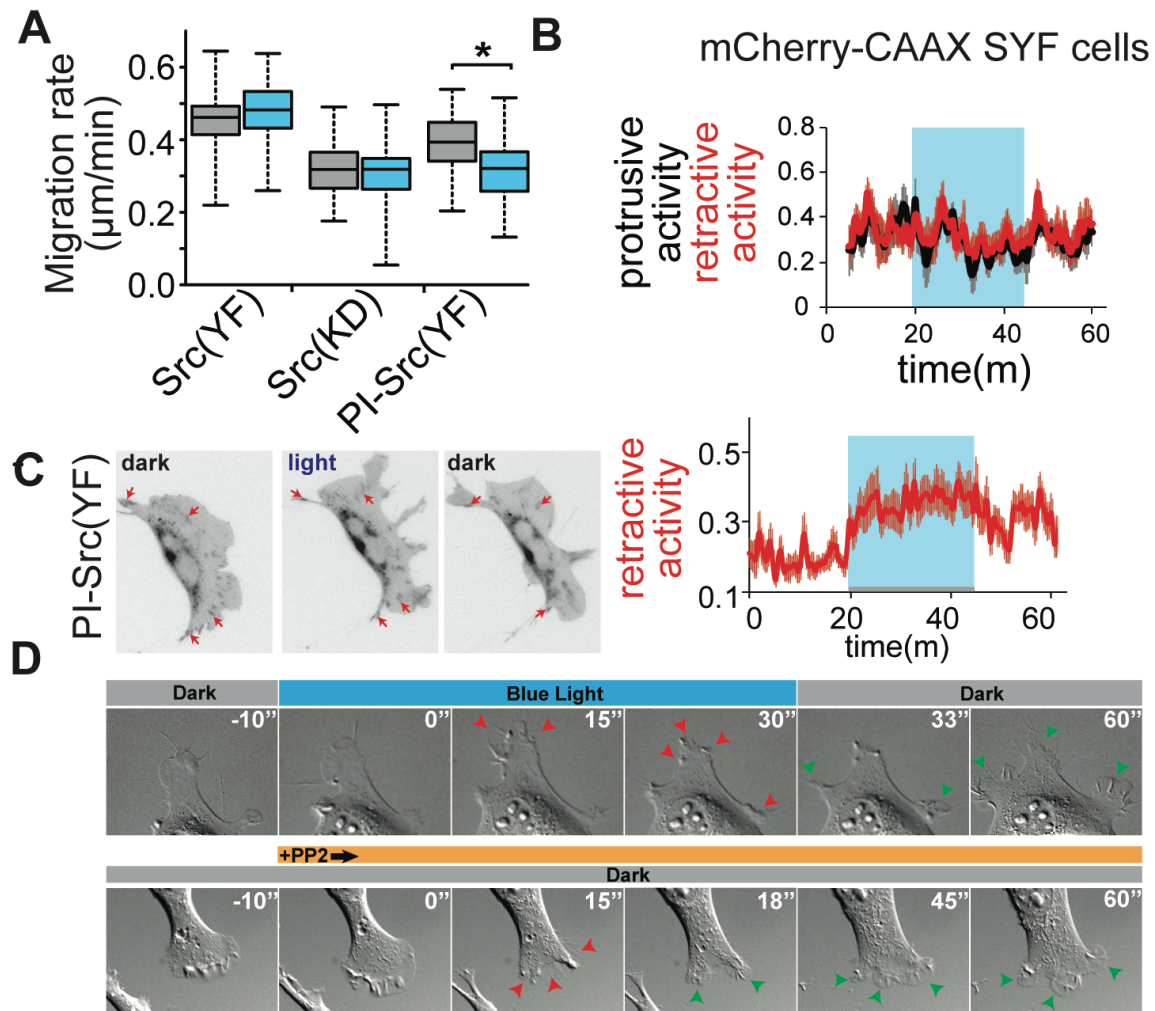


**Fig. S5. The effects of PI-Src and the Src inhibitor PP2 on the motility of SYF cells.**

(A) In a wound healing assay, light alone had no significant effect on the directed migration of cells expressing constitutively active Src (YF) or kinase dead Src (KD). In contrast light impaired the migration of cells expressing PI-Src. The bottom and top of each box indicate 25% and 75% quartiles, respectively.  $p<0.05$  ( $n=80$ ). (B) Protrusive (black) and retractive (red) behavior of control SYF cells expressing the plasma membrane marker mCherry-CAAX. Grey and red shadows indicate error, s.e.m. ( $n=9$ ). (C) (Left) A representative SYF cell expressing PI-Src(YF)-mCherry, which was localized to focal adhesions independent of light; (right) protrusive and retractive behavior of cells expressing PI-Src(YF). Red shadow shows error, s.e.m. ( $n=17$ ). (D) Light or PP2 inhibitor induced shrinkage in cells expressing PI-Src(YF). The retractions extended again when light is removed. For PP2, the effect of the inhibitor limited to 15-20 minutes, after which cells again protruded.

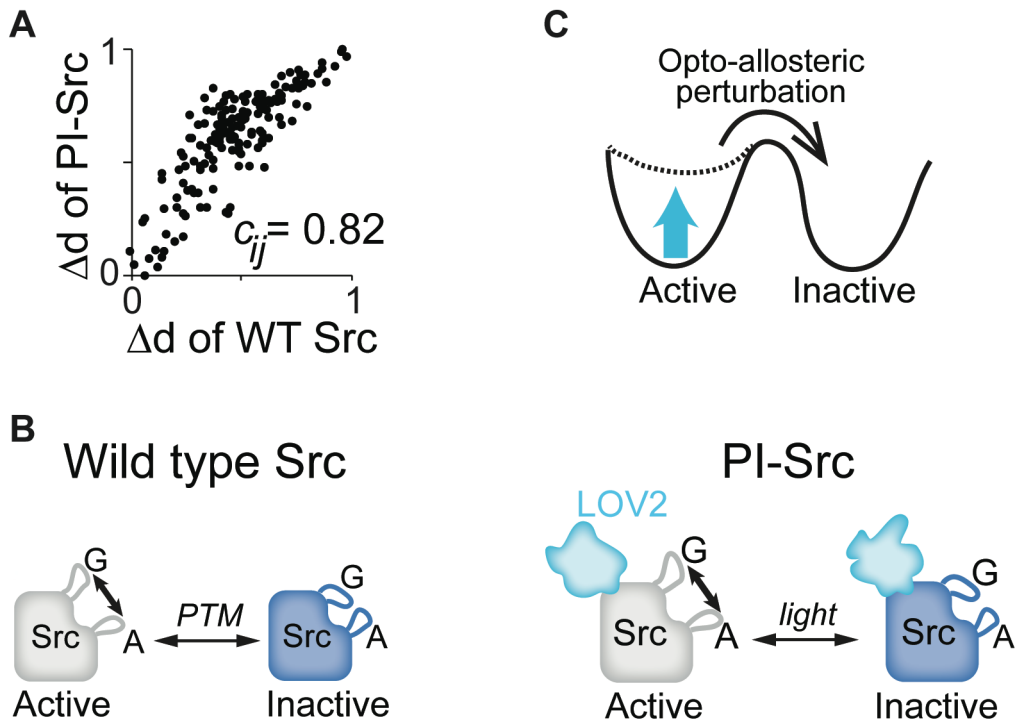


**Fig. S6. Conformational change of WT Src and PI-Src.** (A) Correlation of PI-Src versus WT-Src conformational changes. Changes in distance between all residues were measured for the active versus inactive states of each protein (residues undergoing substantial changes are marked in the black box on the map in Fig. 1D). (B) In WT-Src, the distance between the ATP binding loop G and activation loop A is decreased in the inactive state. (C) A similar conformational change was observed in PI-Src upon irradiation (see Fig. 1D).

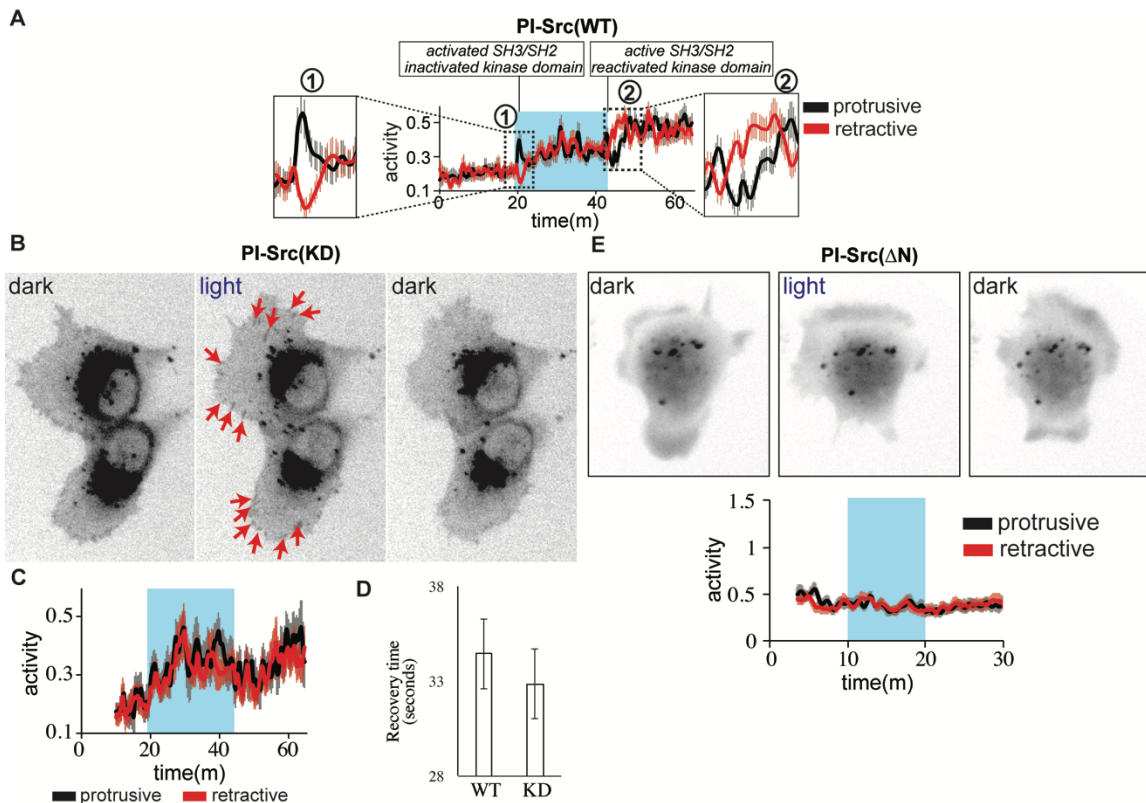


**Fig. S7. PI-Src reversibility, and light-induced morphodynamic changes of SYF cells expressing PI-Src.** (A) In SYF cells expressing PI-Src(WT), PI-Src(WT) reversibly translocates to focal adhesions upon irradiation (see Fig 1E). This is accompanied by changes in protrusive and retractive activity. Note how there is a brief imbalance between these activities both when the cells are first irradiated, and when the light is turned off. In the latter case, retractive activity predominates, leading to a marked contraction when light is removed. (blue = irradiation, black = protrusion, red = retraction). Data are represented as mean + s.e.m (n=18). (B) PI-Src(KD) translocates to peripheral focal adhesions (red arrows) upon irradiation, and (C) SYF cells expressing PI-Src(KD) increase protrusive and retractive activity upon irradiation. Gray and red shadows indicate error, s.e.m. (n=11). (D) Both PI-Src(WT) and PI-Src(KD) relocate from the focal adhesions in 30-40 seconds when the light is turned off. Error bars indicate standard error, s.e.m. (n=18 for WT; n=7 for KD). (E) (Top) PI-Src( $\Delta$ N), a version of PI-Src in which all residues from 248 to the N terminus have been removed (including removal of the SH2 and SH3 domains), does not translocate to focal adhesions upon irradiation (14 cells out of 14 cells); (bottom) SYF cells expressing PI-Src( $\Delta$ N) do not change protrusive or retractive activity upon irradiation. Data are represented as mean + s.e.m (n=15).

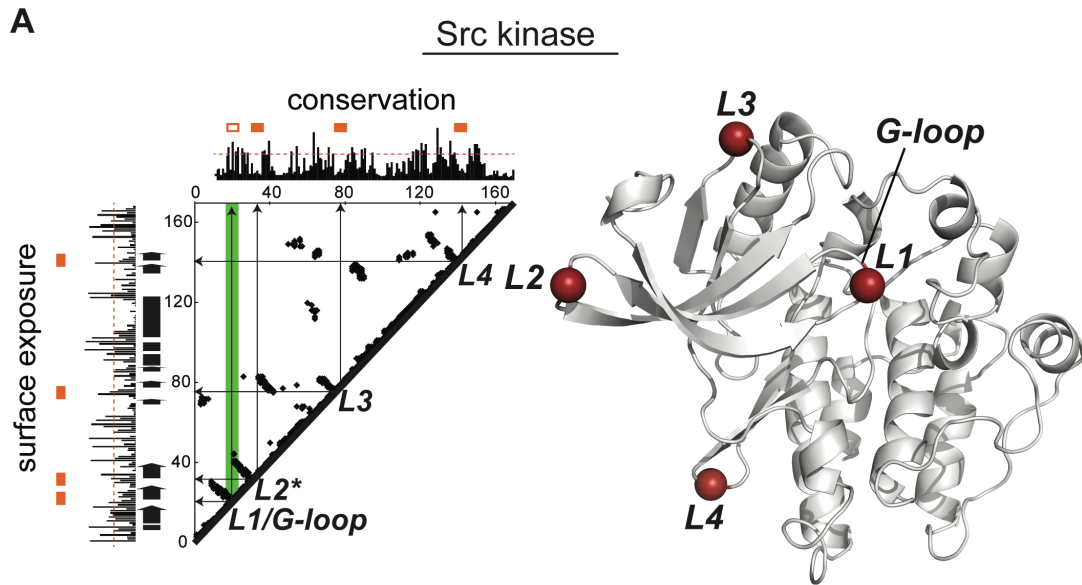


**Fig. S8. Analyzing the insertion loop used in Src kinase.** (A) (Left) The contact map shows the surface exposure and sequence conservation indices of loops in the kinase domain. The filled and unfilled orange boxes show acceptance or rejection based on sequence conservation and surface exposure. Red dashed lines indicate thresholds for acceptance. (Right) All potential loops are shown on the kinase structure. The L2 loop, part of a structural unit that is coupled to the active site, was used as the insertion loop.

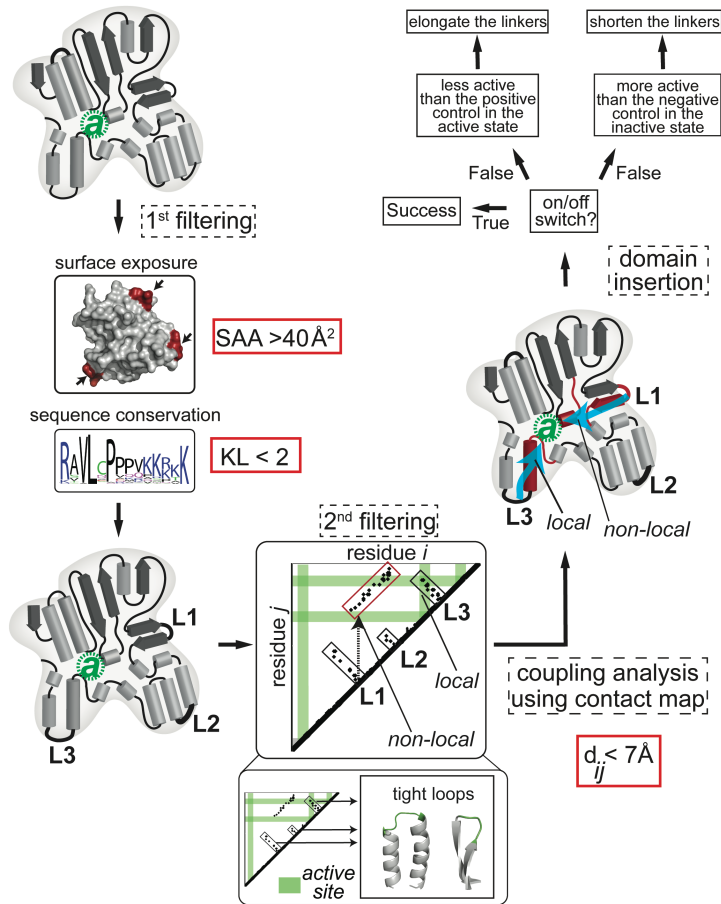


**Fig. S9. Generation of protein switches.** When generating protein switches, the first step is identifying loops that are evolutionary non-conserved and surface-exposed (1<sup>st</sup> filtering). Domain sequences from multiple species were obtained from Pfam (54). Sequence conservation was determined by Kullback-Leibler (KL) conservation, calculated using MISTIC (55). The residues that have KL values lower than 2 were considered non-conserved. Surface exposure was calculated using residue solvent accessible area (SAA), calculated using Stride (53), which was also used to assign the loops (consisting of at least two residues). The residues that have SAA values higher than  $40\text{ \AA}^2$  were considered surface-exposed. Coupling analysis (2<sup>nd</sup> filtering) was performed using contact maps or dynamic coupling maps (not shown here). On contact maps, residue contacts ( $<7\text{ \AA}$ ) extending perpendicular to the diagonal line indicate two interacting structural units connected by a “tight loop”. If this set of contacts reached the active site (green band) in the contact map, the loop was accepted as a potential allosterically coupled loop. Such coupling can be mediated by local interactions (residues that are close in sequence) or non-local interactions (residues that are distant in sequence). Here all three filtered loops are tight loops. L3 is directly coupled to the active site through local contacts, while L1 is indirectly coupled to the active site through non-local interactions. If the initial design did not produce an on/off switch, linker optimization was performed by elongation (by adding flexible residues, e.g. glycine and serine, into the linkers) or shortening (by removing residues from the insertion loop).

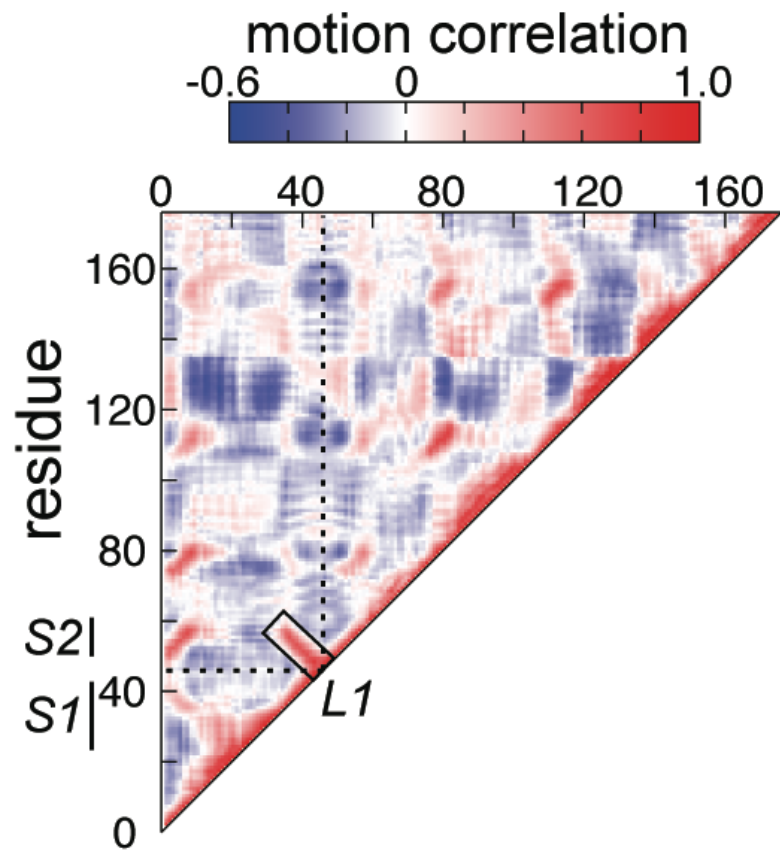


**Fig. S10. Dynamic coupling analysis of Rac1.** Red denotes positive correlation, blue denotes negative correlation. S1 and S2 denote switch 1 and 2 regions. Sets of contacts that substantially correlate (black box) perpendicular to the diagonal line were also captured in static contact map analysis (shown in Fig. 2A).

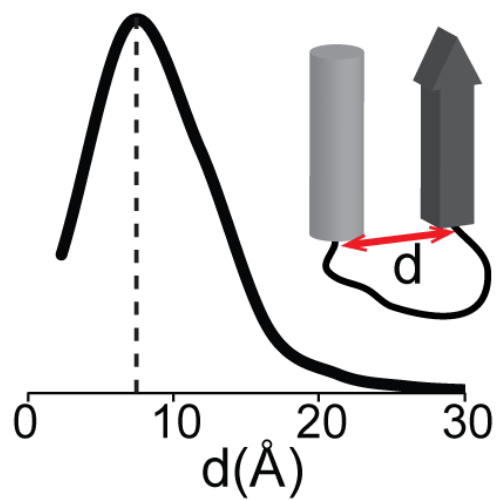


**Fig. S11. Loop distances in the Protein Data Bank.** Distances ( $d$ ) of all loops in all protein structures available in the Protein Data Bank were obtained from the ArchDB server (57).

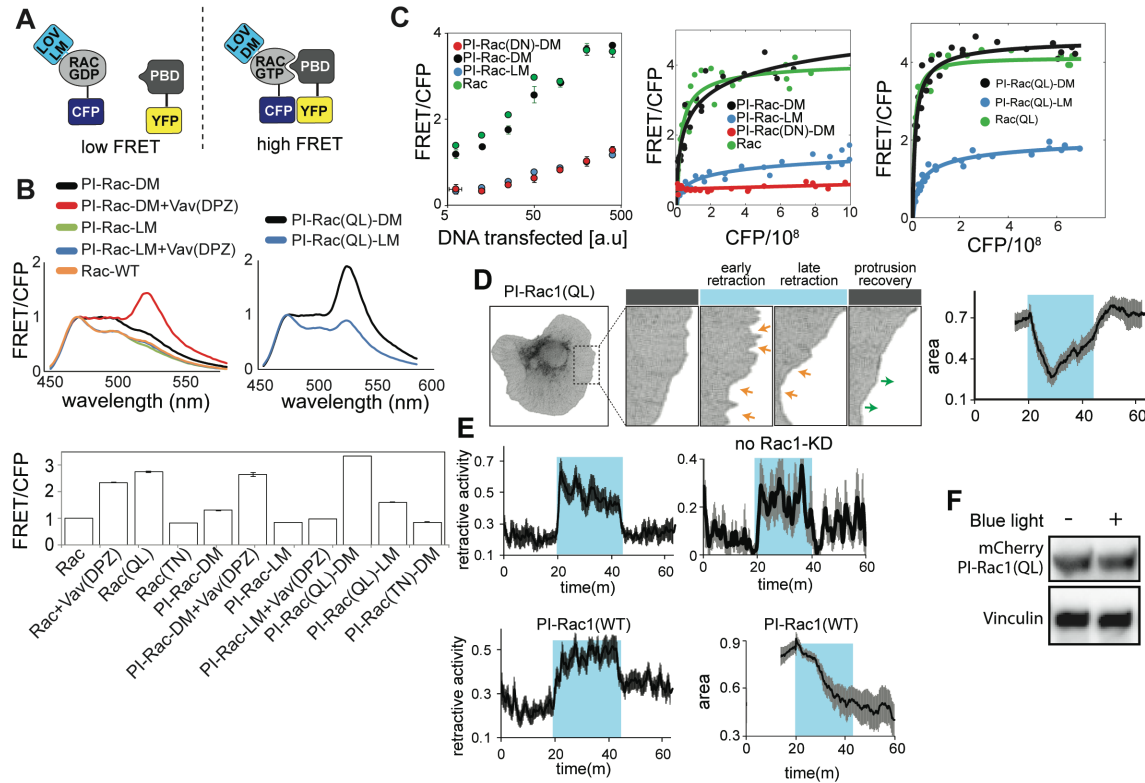


**Fig. S12. Design of PI-Rac1 and photo-inhibitor of PI-Rac1 in living cells.** (A) A modified dual chain FRET biosensor was built to test the activity of PI-Rac1 in living cells. Active Rac1 interacts with the effector protein binding domain (PBD) of PAK1, resulting in FRET from donor cyan fluorescent protein (CFP) to acceptor yellow fluorescent protein (YFP). (B) Fluorescence emission of cell suspensions expressing the biosensor construct showed that PI-Rac (WT) (left) and PI-Rac(QL) (right) were both inhibited in the lit state. All values were normalized to have equal peak CFP emission (473 nm). Control constructs of PI-Rac1 were tested by monitoring the ratio of FRET emission (525 nm) to CFP emission (473 nm) in the same assay. (C) PI-Rac1 was tested using a high-content live cell FRET imaging assay (see Materials and Methods). CFP on the X axis reflected the expression level of the biosensor. At low biosensor concentrations, FRET was not saturated. Titration was used here to find the plateaus indicating maximal FRET (LM = lit state mutant, DM = dark state mutant, QL = constitutively activating mutant Q61L, TN = dominant negative mutant T17N, Vav(DPZ) = truncated constitutively active mutant of Vav2). Error bars represent s.e.m. ( $n=3$ ) from three independent cell populations. (D) Upon irradiation, fibroblasts expressing PI-Rac1(QL) retracted (orange arrows), then respread (green arrows). (E) (Top) Quantifying the cell retraction induced by irradiation of fibroblasts expressing PI-Rac1(Q61L) with ( $n=11$ ) and without ( $n=9$ ) Rac1 knock-down (KD). (Bottom) Cells expressing PI-Rac1(WT) also retracted upon irradiation. (Blue box = irradiation, gray envelope = s.e.m.). (F) Protein levels of mCherry tagged PI-Rac1(QL) were determined using anti-mCherry antibody. Vinculin is a loading control.

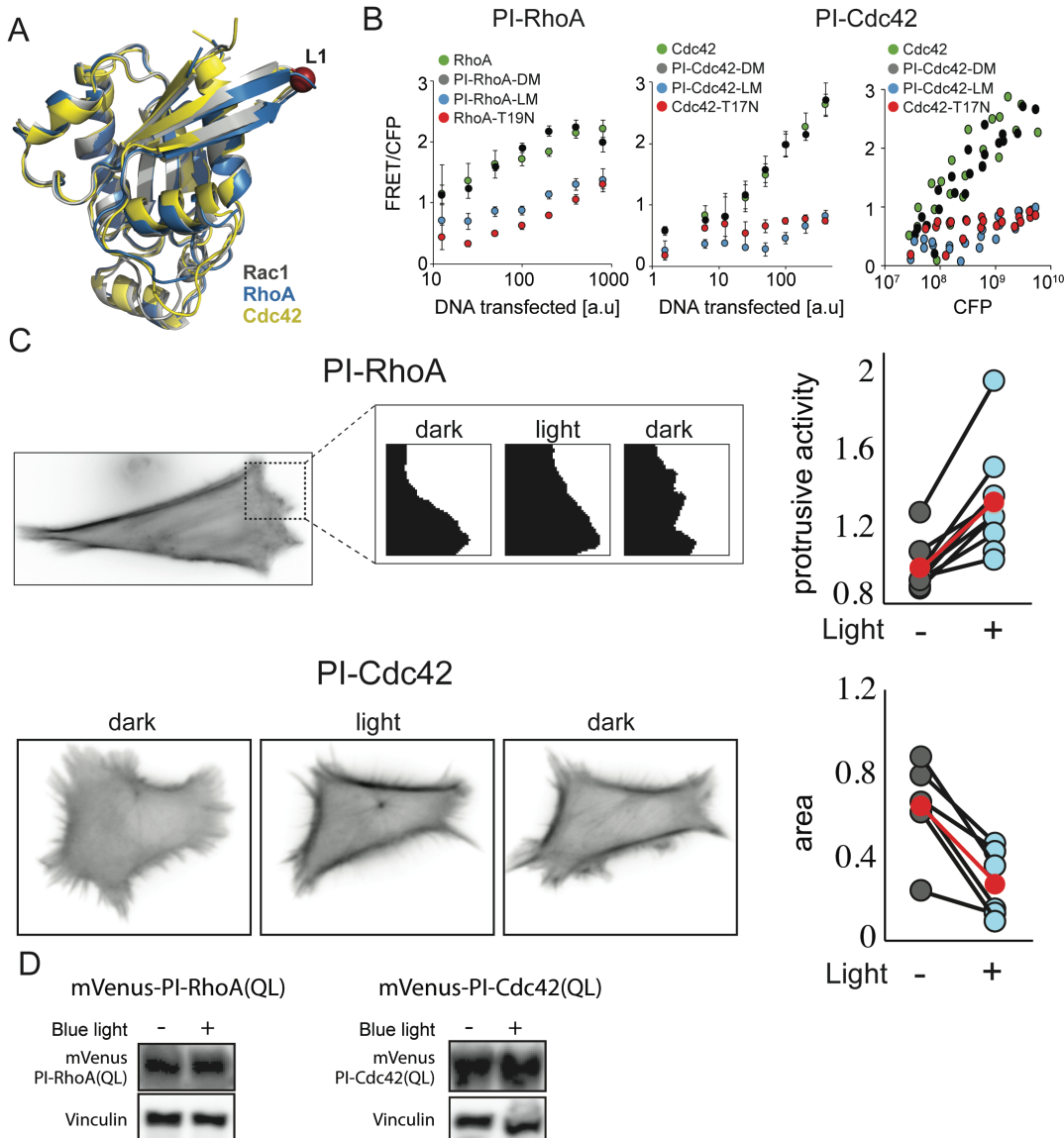


**Fig. S13. PI-RhoA and PI-Cdc42 examined in live cells** (A) A loop homologous to that targeted in Rac1 was used to build PI-RhoA and PI-Cdc42. (pdb id of Rac1: 1foe; pdb id of RhoA: 1x86; pdb id of Cdc42: 1cee). (B) Dual chain FRET biosensors were built to test the activity of PI-RhoA and PI-Cdc42, as in fig. S12. DM and LM denote dark and lit mutants. T19N is a dominant negative mutation. For PI-Cdc42, as with WT Cdc42, expression above certain levels led to extensive cell retraction, preventing us from reaching assay concentrations at which activity plateaued. CFP represents expression levels. Error bars represent s.e.m. ( $n=3$ ) from three independent cell populations. (C) Mouse embryonic fibroblasts that expressed PI-RhoA ( $n=10$ ) showed increased protrusions upon irradiation. Irradiation of cells expressing PI-Cdc42 ( $n=6$ ) produced retraction and an accumulation of actin at the cell periphery. Red lines indicate the mean. Cells were visualized using Lifeact-mCherry. (D) Protein levels of mVenus tagged PI-RhoA(QL) and PI-Cdc42(QL) were detected using anti-GFP (JL8) antibody. Vinculin is a loading control.

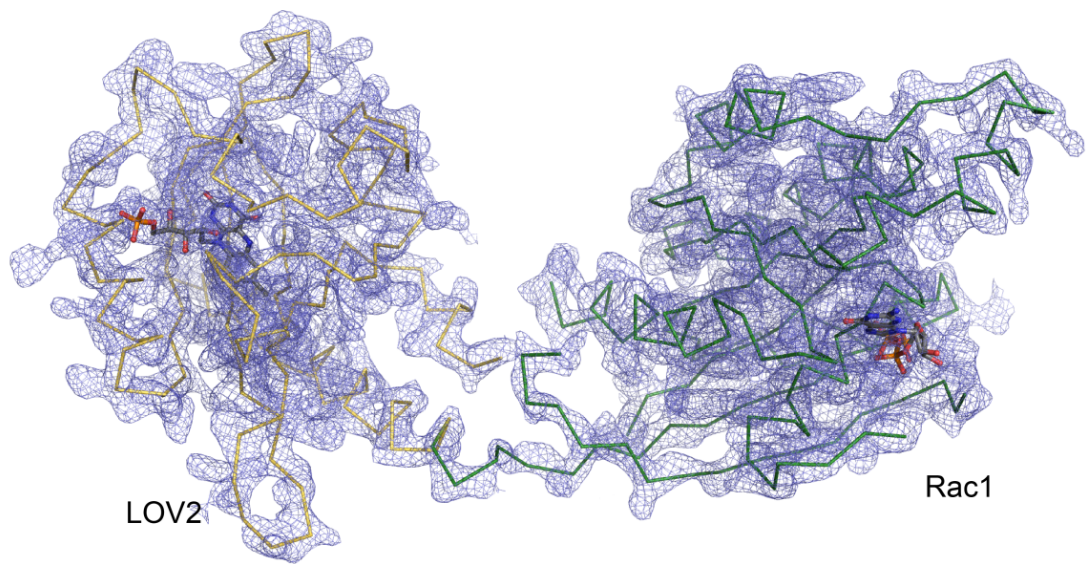


**Fig. S14. Electron-density map and refined model of PI-Rac1 (C450A).** The  $2F_o - F_c$  map is contoured at  $1.0\sigma$ . Water molecules and ions are not shown for clarity.

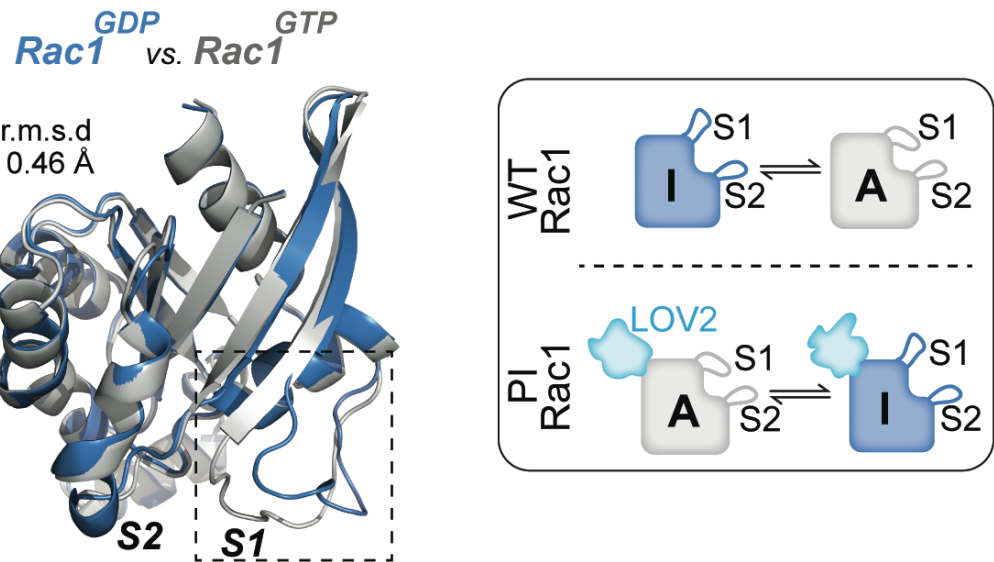


**Fig. S15. Comparison of inactive and active states of Rac1.** (Left) Inactive (blue, pdb id: 1i4d) and active states (gray pdb id: 4gzl) of Rac1 were superimposed. The largest conformational change occurs in the switch 1 (S1) and switch 2 (S2) regions. Root mean square deviation (RMSD) between the two conformations is 0.46 Å. (Right) WT Rac1 and PI-Rac1 undergo similar conformational changes. The distance between S1 and S2 is decreased in the active state (A, gray) and increased in the inactive state (I, blue).

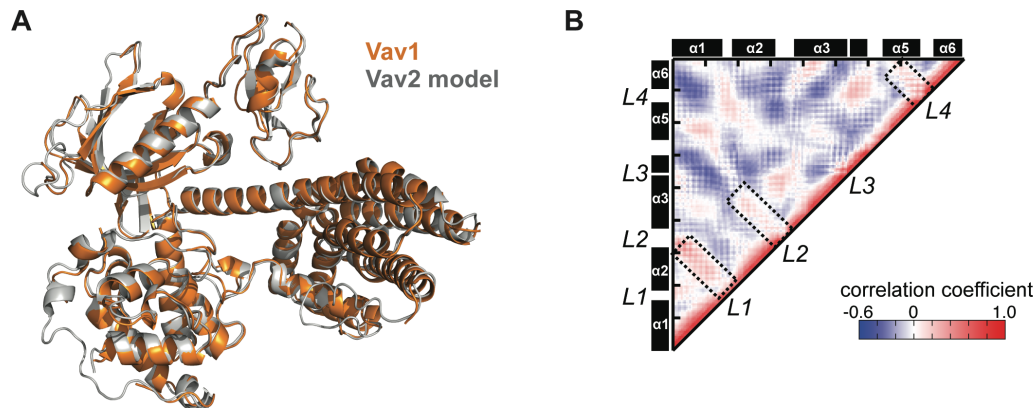


**Fig. S16. Structural analysis of Vav2.** A structural model of Vav2 was built based on the crystal structure of Vav1 (pdb id: 3ky9), and then simulated using discrete molecular dynamics to obtain dynamic coupling, shown with a correlation map (right). Sets of contacts that substantially correlate (black dashed boxes) perpendicular to the diagonal line were also captured in static contact map analysis (shown in Fig. 3A). Red denotes positive correlation, blue denotes negative correlation.

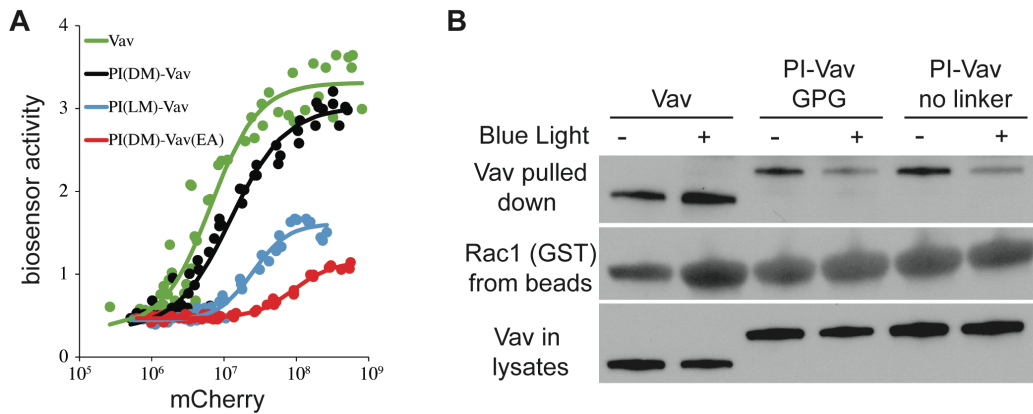


**Fig. S17. Testing PI-Vav2 with high-content microscopy and pull-down assays.** (A) A Rac1 biosensor was used as a readout to examine PI-Vav2 activity in living cells. Vav2 expression level (x-axis) was determined using the fluorescence intensity of mCherry tagged to Vav2 constructs. Error bars represent s.e.m. ( $n=3$ ) from three independent cell populations. DM and LM denote dark and lit mutants. EA denotes E200A/K333A catalytically inactive mutation. (B) Biochemical GEF activity assays were performed using purified GST-Rac1(G15A) mutant as a pulldown reagent (see Materials and Methods). Both PI-Vav2 designs (without a linker or with a GPG linker at the termini of LOV2) showed inhibition with light.

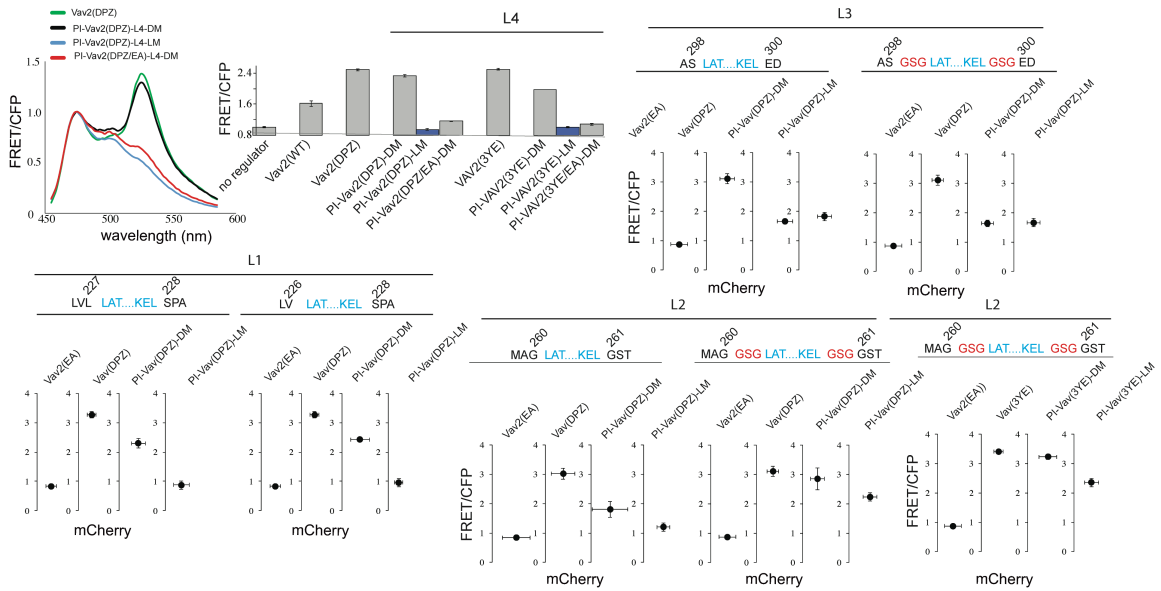


**Fig. S18. Testing PI-Vav2 in living cells using a Rac1 biosensor.** The Rac1 biosensor was co-expressed with PI-Vav2 or control constructs. Fluorescence emission of cell suspensions expressing the biosensor construct showed that wild type (WT) Vav2, a truncated activated version of Vav2 consisting of DH-PH-Zinc Finger domains (DPZ), and activated full length Vav2 with a triple phospho-tyrosine mutation (3YE) are all capable of activating Rac1. Both full length (3YE) or truncated versions (DPZ) of PI constructs were inhibited in the lit state (blue). There are 4 non-conserved and surface exposed loops. L1, L2, and L4 are tight, unlike L3 which consists of only a single residue and does not connect two interacting structural units (see Fig. 3A). Consistent with this, LOV2 insertion at L3 inactivated Vav2 and did not produce a switch. L4 (without any attempted optimization) and L2 (with linker optimization) both produced efficient switches, whereas L1 (without any linker optimization) displayed less efficient switching. EA denotes E200A/K333A catalytically inactive mutations. Error bars represent s.e.m. ( $n=3$ ) from three independent cell populations.

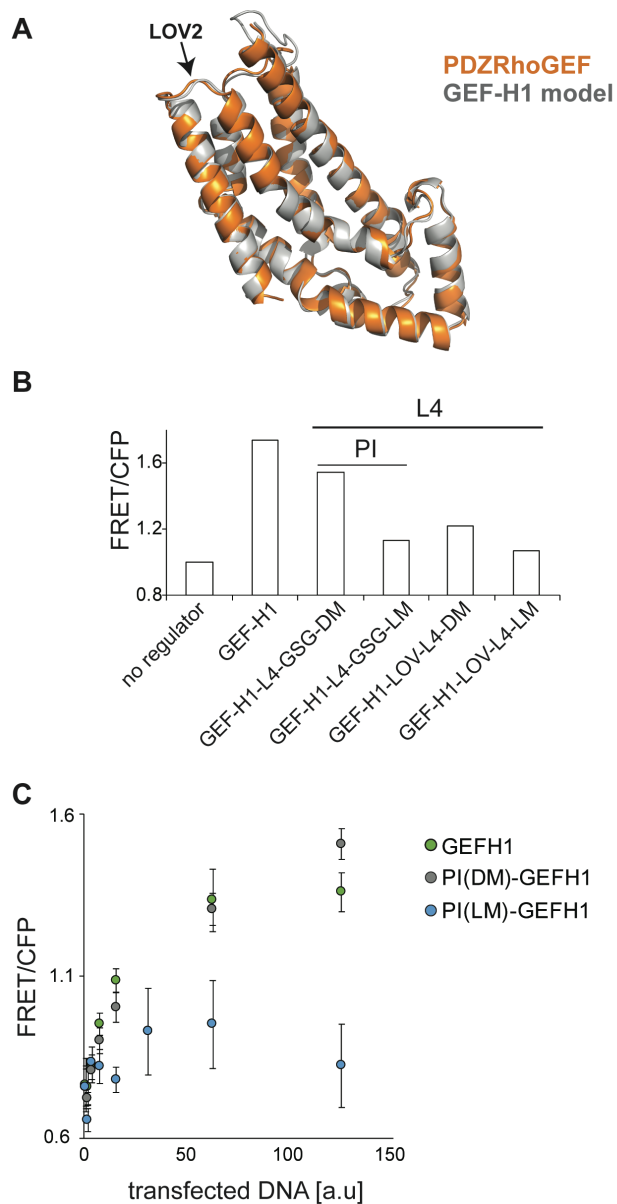


**Fig. S19. Testing PI-GEF H1 in living cells using a RhoA biosensor.** (A) A structural model of GEF-H1 was built based on the crystal structure of PDZ Rho GEF (pdb id: 3t06). (B) Fluorescence emission of cell suspensions expressing the biosensor showed that PI-GEF-H1 was inhibited in the lit state. Addition of a GSG linker between LOV2 and the DH domain increased the dynamic range substantially (C) PI-GEF-H1 was tested using a high-content live cell FRET imaging assay (see Materials and Methods). The bar graph (right) was constructed based on the concentrations at which activity plateaued. DM and LM denote dark and lit mutants. Error bars represent s.e.m. ( $n=3$ ) from three independent cell populations.

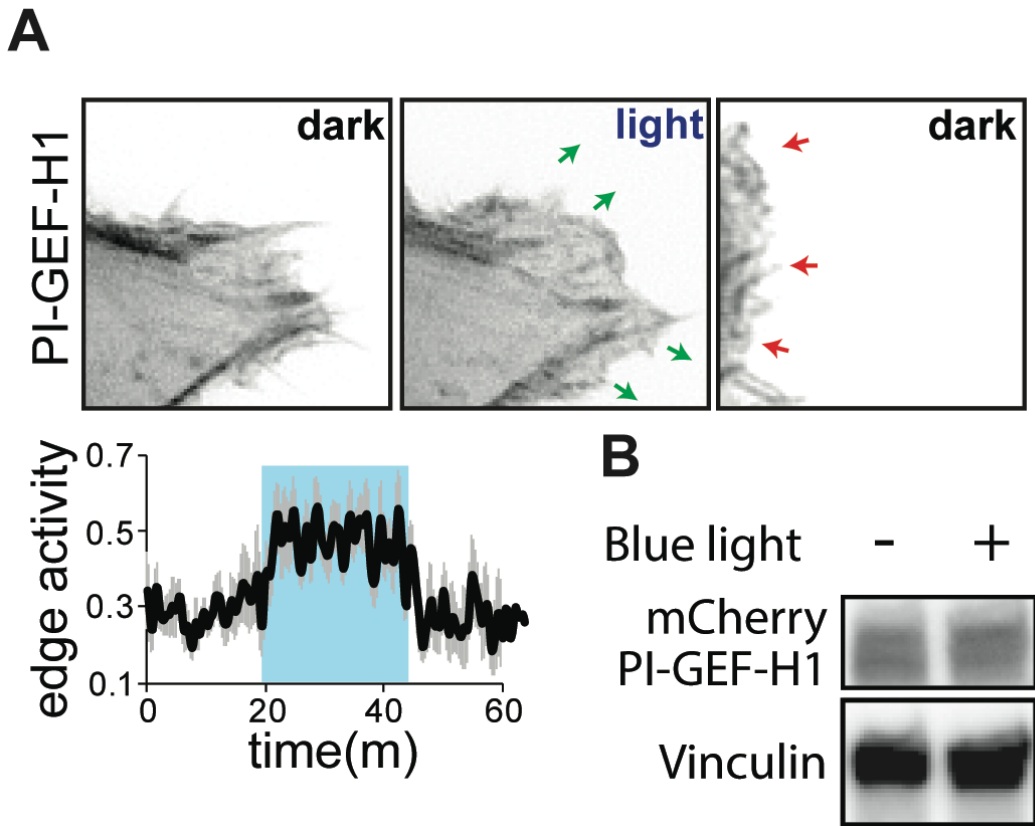


**Fig. S20. Photo-inhibition of PI-GEF-H1 in living cells.** (A) (Top) A HeLa cell showing rapid protrusions with irradiation, and shrinkage upon returning to the dark; (bottom) The cell edges became more active during irradiation, with more frequent oscillations. The graph shows quantification of overall edge activity (combination of both protrusive and retractive activity). Gray shade indicates error, s.e.m. ( $n=8$ ). (B) Irradiation (1 hour) does not change the expression of PI-GEF-H1. Protein level of mCherry tagged, irradiated and non-irradiated PI-GEF-H1 were detected using anti-mCherry antibody. Vinculin is a loading control.

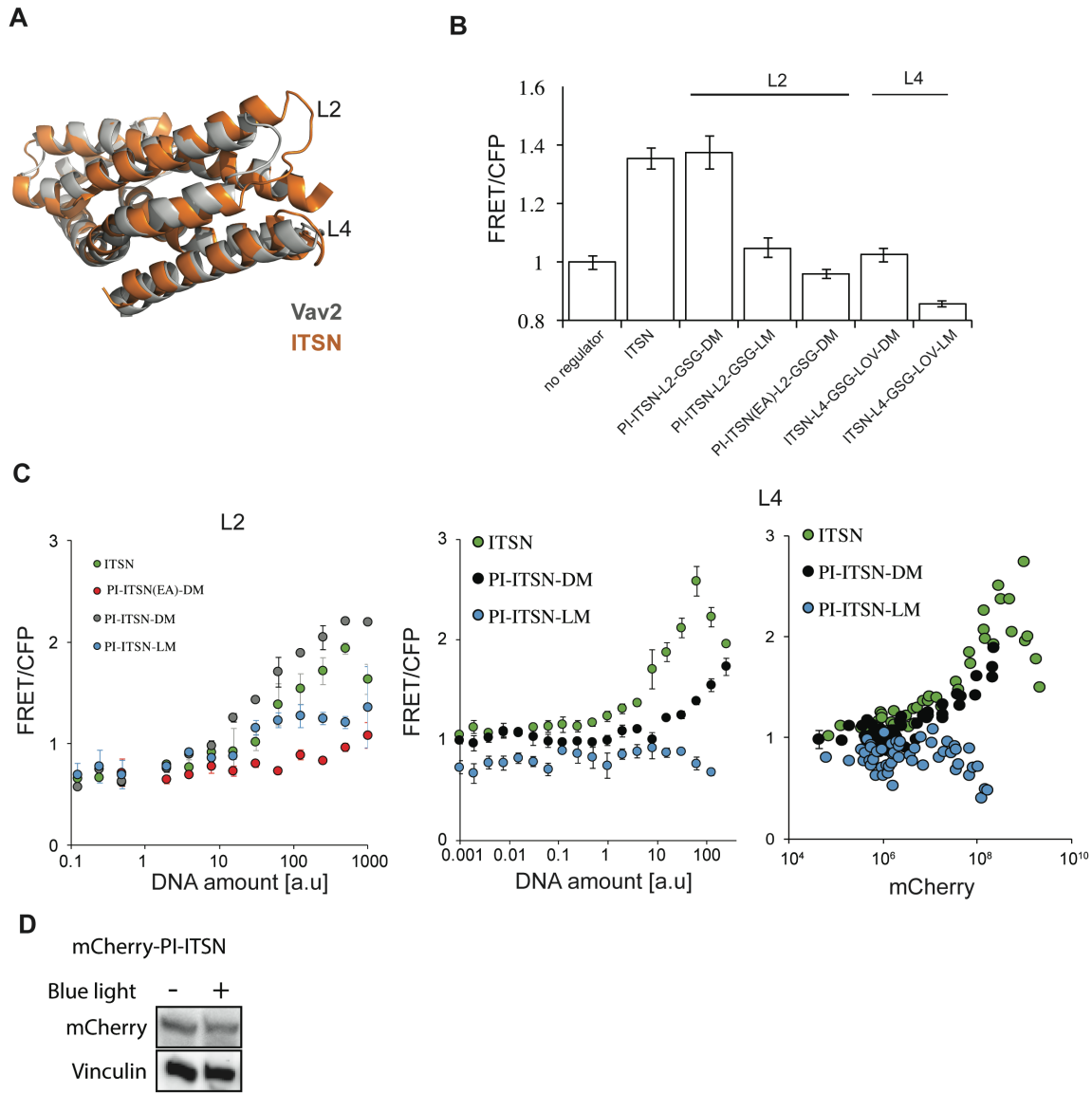


**Fig. S21. Testing PI-ITSN in living cells using a Cdc42 biosensor.** (A) (Left) Crystal structure of ITSN superimposed on the model of Vav2; (right) testing ITSN with LOV2 inserted at loops L2 and L4, using the fluorometer assay. (B-C) Fluorescence emission of cell suspensions expressing the biosensor showed that PI-ITSN (L2) produced a more effective switch than PI-ITSN (L4). (C) ITSN-LOV fusions were also tested using the high-content live cell FRET imaging assay (see Materials and Methods). mCherry, fused to the PI-ITSN, indicates expression levels. Error bars represent s.e.m. ( $n=3$ ) from three independent cell populations. (D) The protein levels of mCherry tagged PI-ITSN in irradiated and non-irradiated cells were detected using anti-mCherry antibody. Vinculin is a loading control.

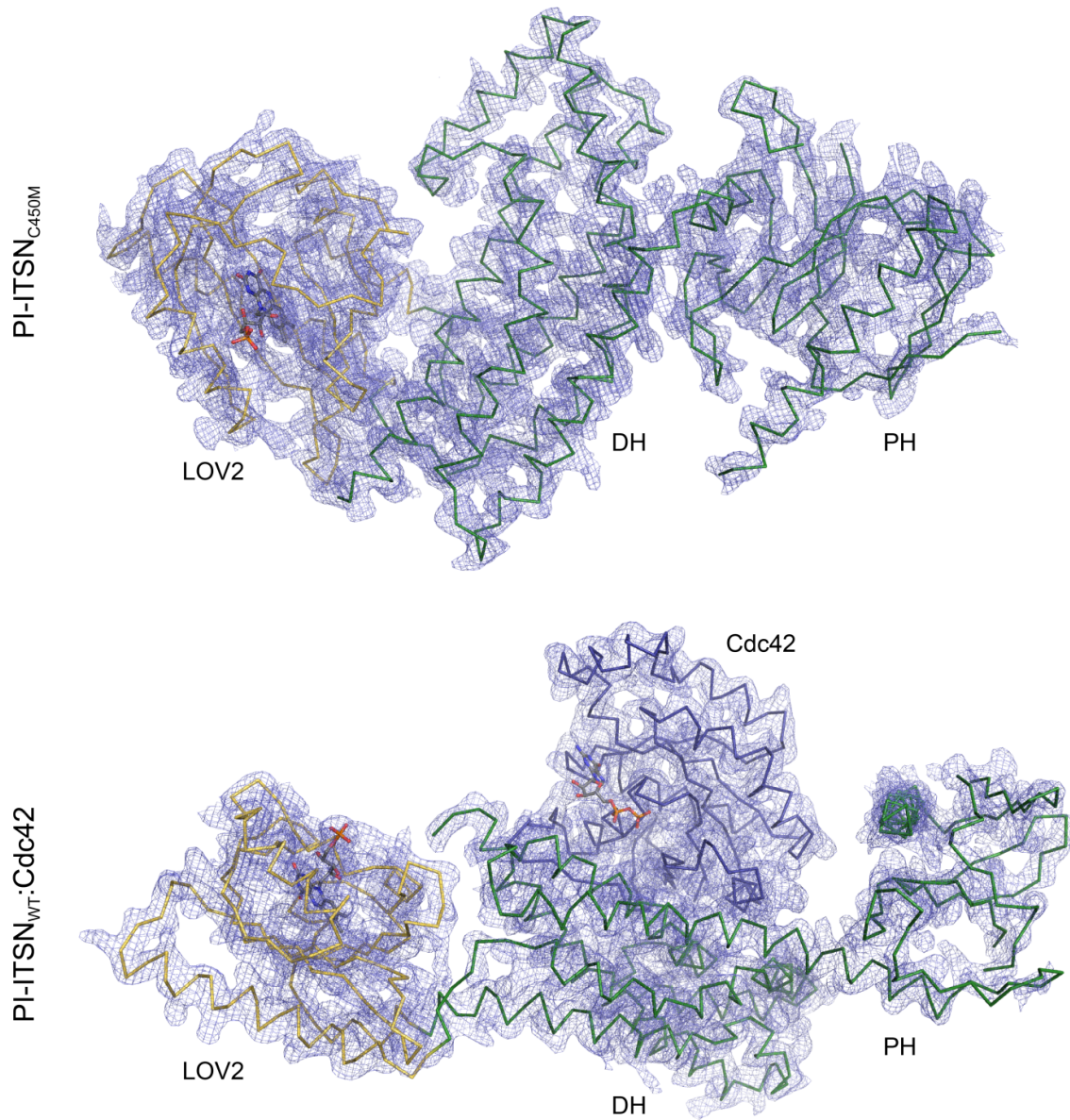


**Fig. S22. Electron-density maps and refined models of PI-ITSN (C450M) and PI-ITSN(WT):Cdc42 complex.** The  $2F_o - F_c$  map is contoured at  $1.0\sigma$ . Water molecules and ions are not shown for clarity.

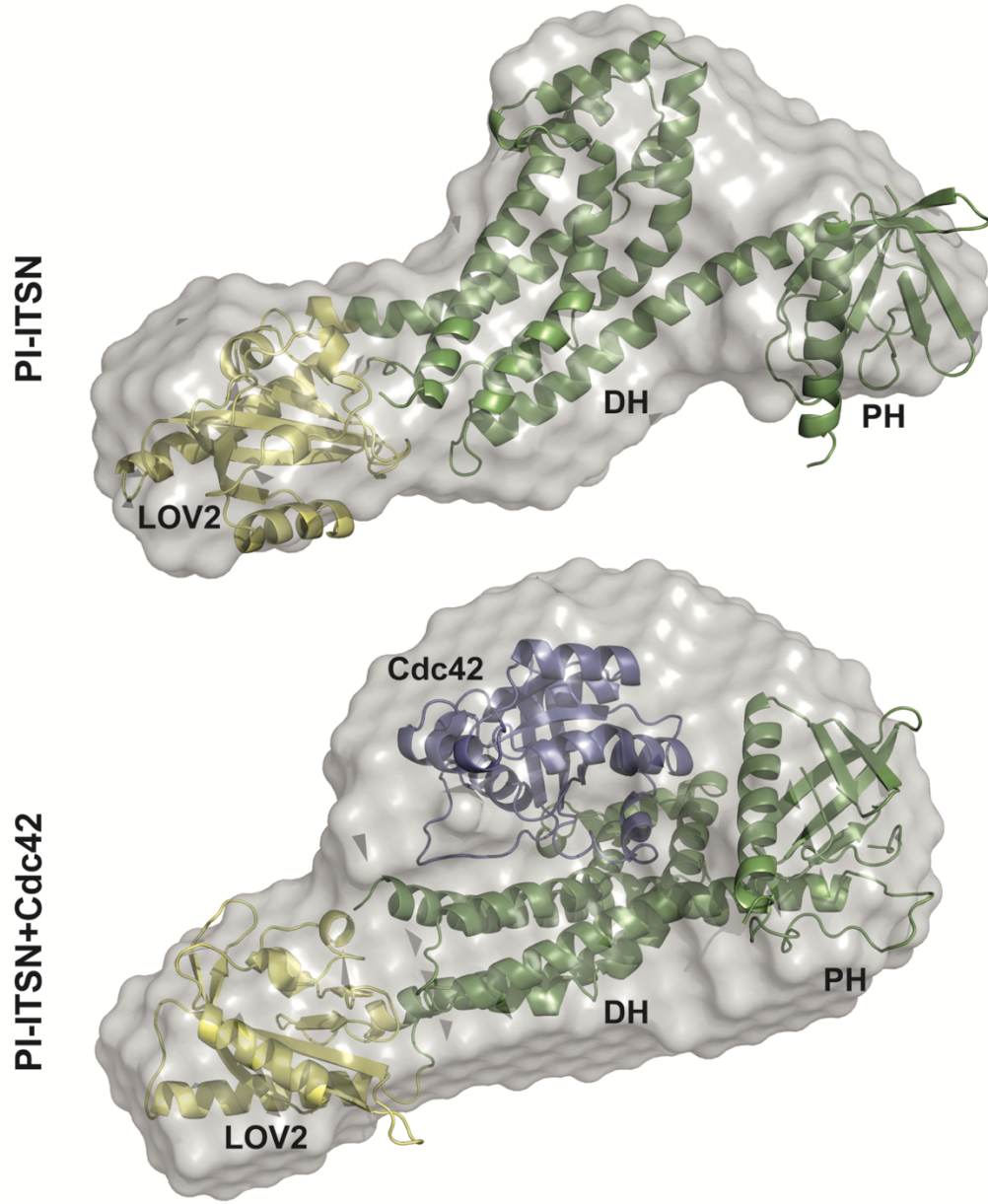


**Fig. S23. Structural characterization of PI-ITSN in solution.** Low resolution structures of PI-ITSN and PI-ITSN:Cdc42 in solution produced by small angle X-ray scattering. Gray cloud is generated by DAMMIF(40), and superimposed on the crystal structures.

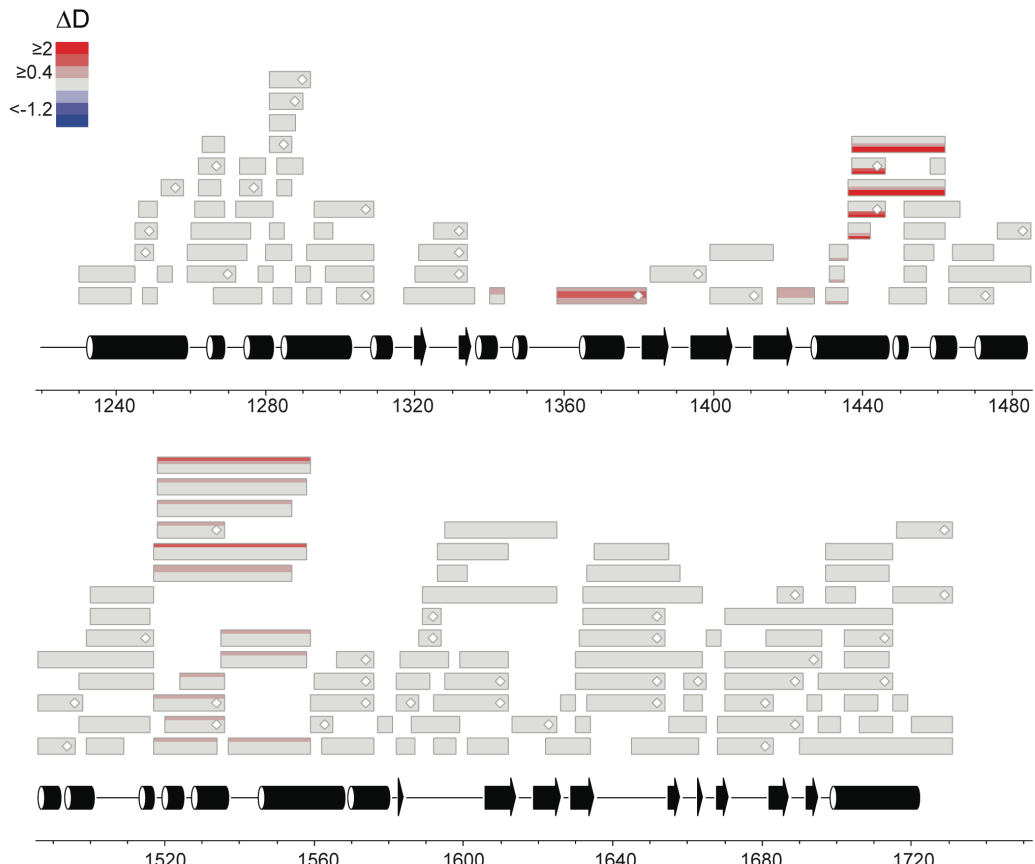


**Fig. S24. Overview of PI-ITSN hydrogen deuterium exchange studies.** Our results show the effect of blue-light illumination on peptide's relative deuterium incorporation ( $D_{\text{rel}}$  of PI-ITSN<sub>light</sub> -  $D_{\text{rel}}$  of PI-ITSN<sub>dark</sub>). Each box corresponds to one peptide and contains five different colors according to the legend for the incubation times of 10, 45, 180, 900 and 3600 s. MS/MS confirmed peptides are marked with white diamonds.

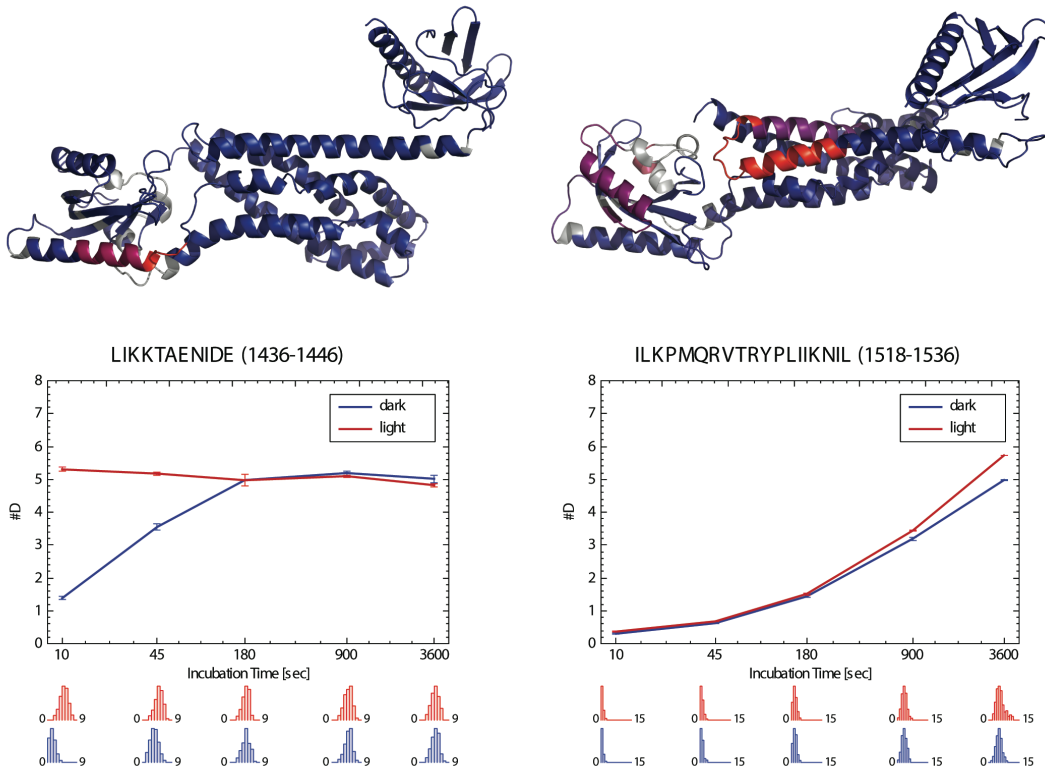


**Fig. S25. Structural elements of PI-ITSN affected by blue-light illumination.** The structures of PI-ITSN are colored according to the differences in relative deuteration upon blue-light illumination, for the 45 s timepoint (left) and 3600 s timepoint (right). Deuterium uptake plots of representative PI-ITSN peptides with  $D_{\text{rel}}$  plotted against deuteration time for two experiments (dark and blue-light conditions). The lower panels show the software estimated abundance distribution of individual deuterated species on a scale from undeuterated to all exchangeable amides deuterated.  $D_{\text{rel}}$  values are shown as the mean of three independent measurements and error bars correspond to the standard deviation.

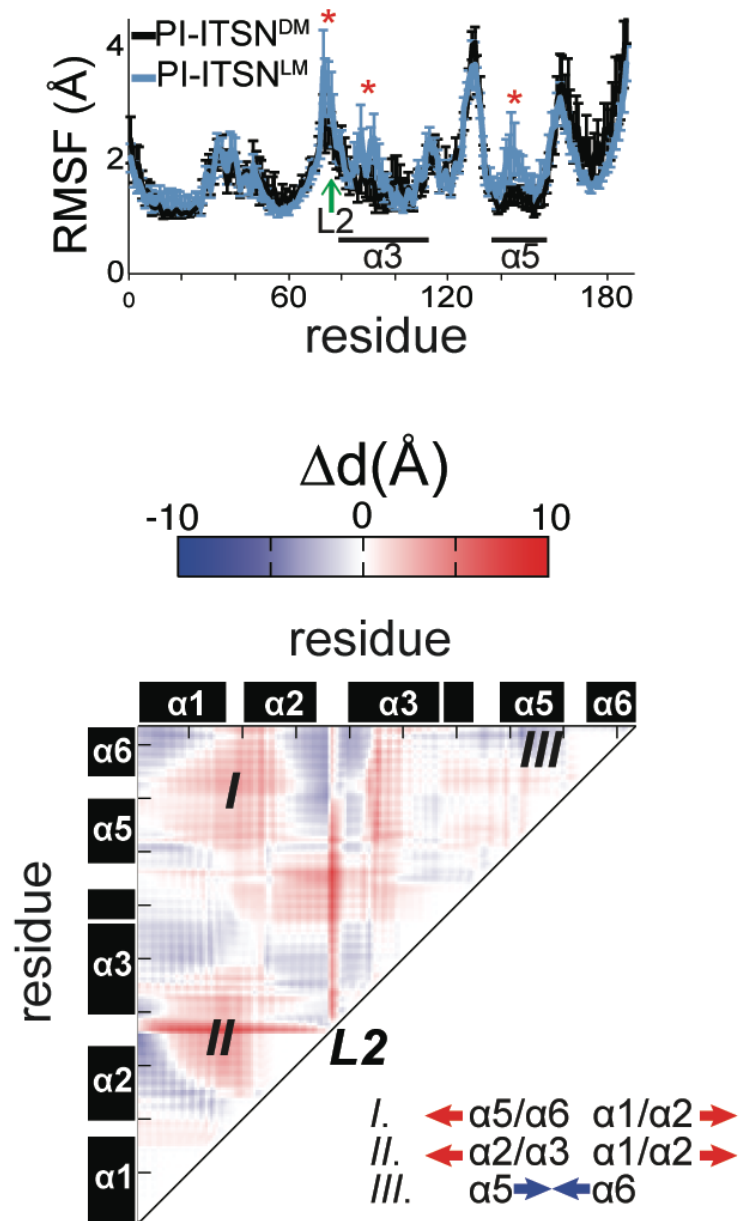


**Fig. S26. Change in the dynamics and conformation of PI-ITSN, estimated from DMD simulations.** (Top) Root mean square fluctuations (RMSF) of the dark-state mutant (DM) and lit state mutant (LM) of PI-ITSN; (bottom) Map of the distance between each  $\alpha$ -carbon of DH domain, showing the conformational change of PI-ITSN. Red denotes the residues that move away from each other, blue denotes the residues that approach each other (blue and red arrows). Error bars represent s.e.m. from five independent trajectories for each condition.

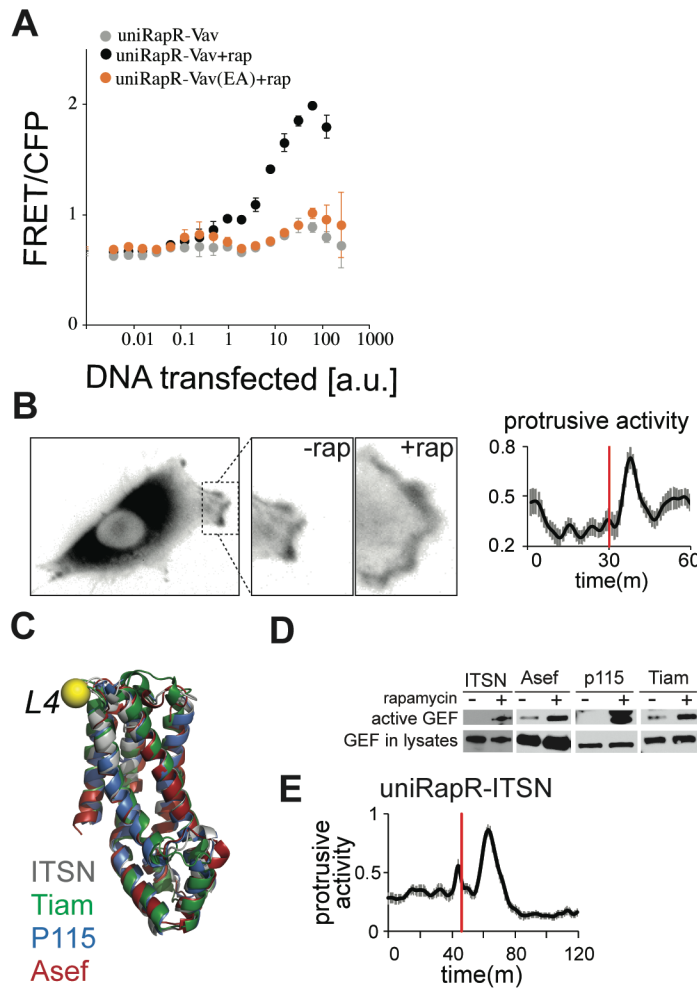


**Fig. S27. UniRapR-GEFs in living cells.** (A) The high-content live cell imaging assay showed rapamycin-dependent activation of uniRapR-Vav2. Titration in the absence and presence of saturating rapamycin (500 nM). Error bars represent s.e.m. (n=3) from three independent cell populations. (B) (Left) A fibroblast expressing uniRapR-Vav2 showed increased protrusive activity upon addition of rapamycin; (right) fibroblasts expressing uniRapR-Vav2 protrude upon addition of rapamycin (red line). Error bars represent s.e.m. (n=16). (C) DH domains of ITSN, Tiam1, p115, Asef share the same fold. The uniRapR domain was inserted at L4 (yellow circle) (D) UniRapR-ITSN, uniRapR-Asef, uniRapR-p115, and uniRapR-Tiam1 show rapamycin-induced activation in GTPase pulldown assays. (E) Starved fibroblasts expressing uniRapR-ITSN protrude upon addition of rapamycin (red line). Error bars represent s.e.m. (n=16).

## Opto-allosteric activation

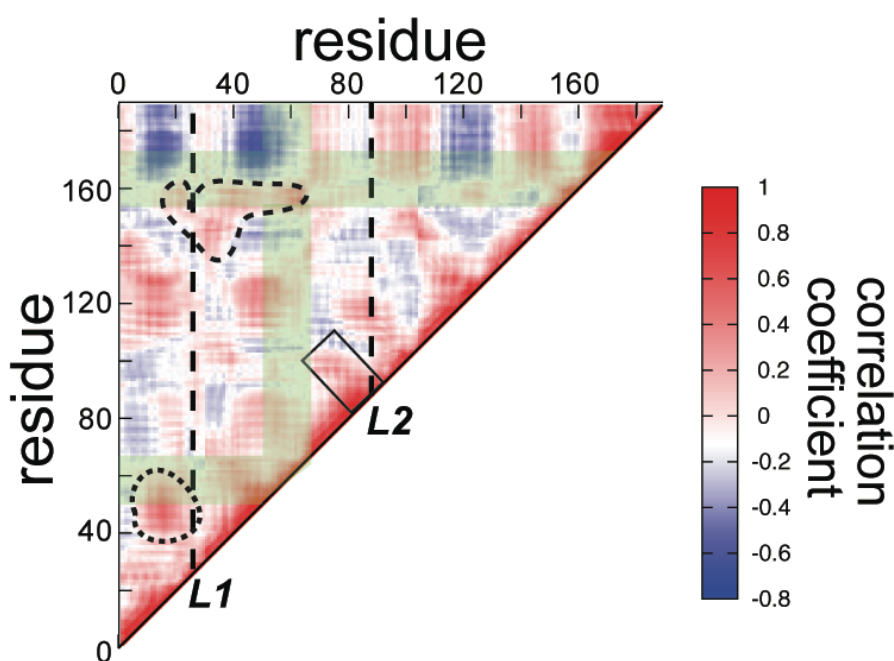
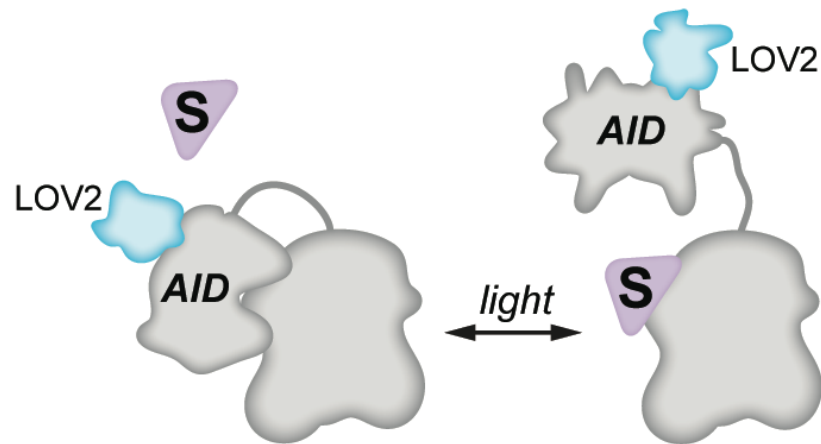


**Fig. S28. Opto-allosteric activation and dynamic coupling analysis of the CH domain.** (Top) Optoallosteric activation can be achieved by targeting an auto-inhibitory (AID) domain for inhibition by LOV2. S denotes substrate or protein target. (Bottom) Dynamic coupling of the CH domain was seen using molecular dynamics simulations. Red denotes positive correlation, blue denotes negative correlation. Insertion of LOV2 into L1 or L2 produced a photo-activatable Vav2 switch. Dashed areas indicate positive correlation between the insertion loop L1 and the active site (green band).

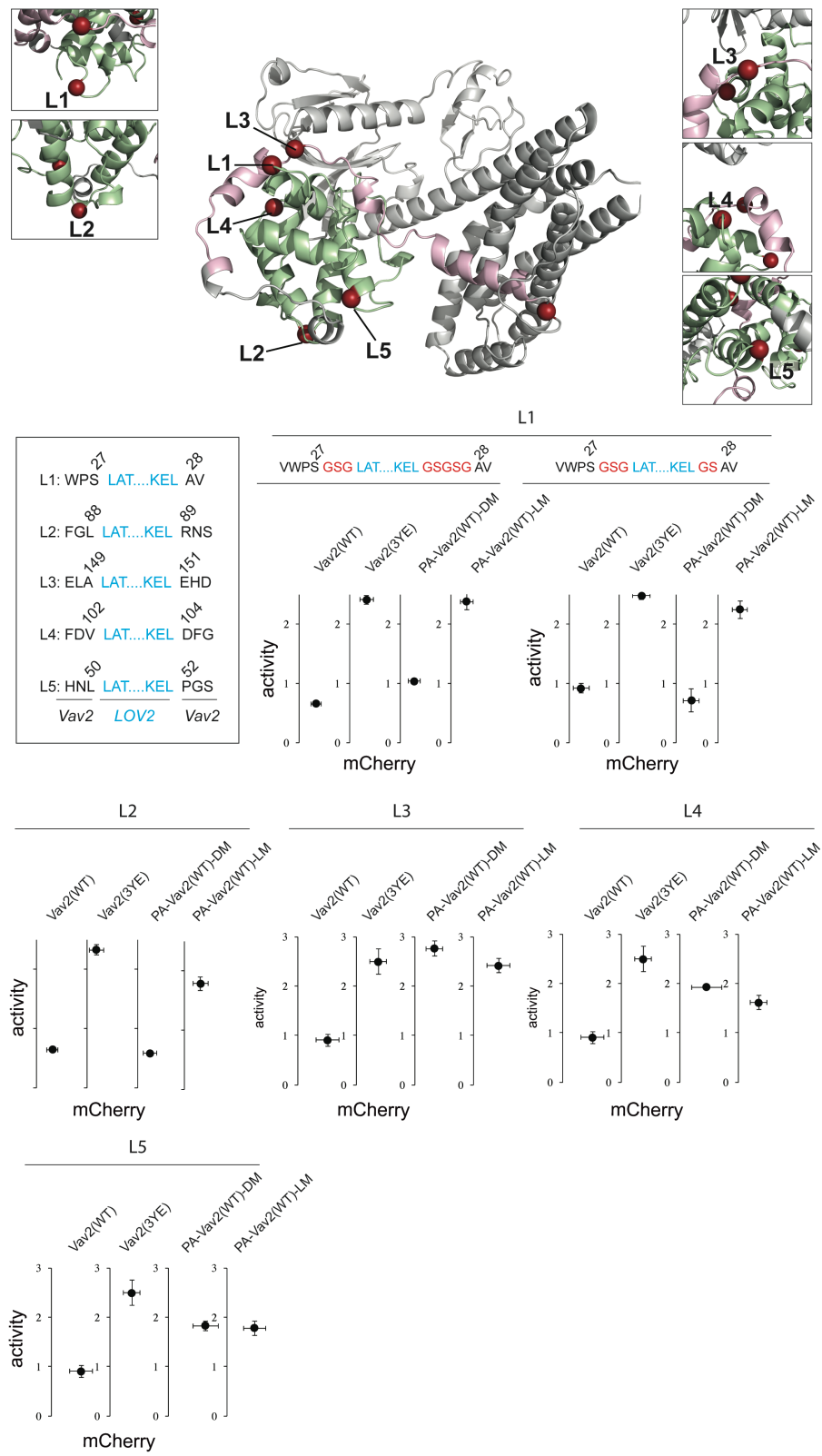


**Fig. S29.** See the next page for the legend.

**Fig. S29. Testing PA-Vav2 in living cells using a Rac1 biosensor.** Five insertion loops (L1-L5) were tested using a high-content live cell FRET imaging assay (see Materials and Methods). L1 (both short and long linker analogs) and L2 produced effective switches. L5 is not surface exposed (see Fig. 4A), so it produced activation in the dark state. L3 and L4 in CH are facing towards the DH and PH domains in full length Vav2 (~10Å L3 and D488 of PH domain and 13Å K485); Because they are not surface-exposed in the context of full-length Vav2, they produced activation in the dark state. Error bars represent s.e.m. (n=3) from three independent cell populations.

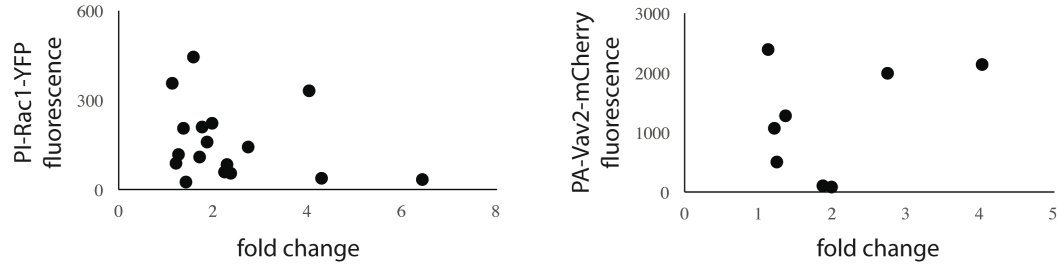


**Fig. S30. Effect of protein expression on the phenotype of cells that express both PI-Rac1 and PA-Vav2.** The behavior of the cells that expressed both PI-Rac1-YFP and PA-Vav2-mCherry was not dependent on the expression level of the PI-Rac1 or PA-Vav2 (Y axes). The phenotype was quantified by monitoring protrusive activity. Average fluorescence intensity after background subtraction was used as a measure of intracellular protein concentration.

**Table S1.**

Crystallography statistics for the dark-state mutant PI-Rac1(C450A). \* Values in parentheses are for the highest resolution shell.

PI-Rac1 <sub>C450A</sub>	
<b>Data collection</b>	
Space group	<i>P</i> 12 <sub>1</sub> 1
Cell dimensions	
<i>a</i> , <i>b</i> , <i>c</i> (Å)	36.1, 74.3, 58.4
$\alpha$ , $\beta$ , $\gamma$ (°)	90.0, 94.6, 90.0
Resolution (Å)	50-2.6 (2.7-2.6)*
No. unique reflections	9516 (1009)*
$R_{\text{merge}}$	0.101 (0.685)*
$I/\sigma I$	14.3 (3.2)*
Completeness (%)	99.8 (100.0)*
Redundancy	6.5 (6.4)*
Wilson B (Å <sup>2</sup> )	48.6
<b>Refinement</b>	
Molecules per a.u.	1
Resolution (Å)	37.1-2.6
No. unique reflections	9506
$R_{\text{work}}/R_{\text{free}}$	0.2063/0.2553
No. atoms	2622
Protein	2529
Ligand/ion	66
Water	27
<i>B</i> -factors	52.1
Protein	52.3
Ligand/ion	47.7
Water	39.6
R.m.s. deviations	
Bond lengths (Å)	0.002
Bond angles (°)	0.610
Ramachandran	
favored (%)	97.5
outliers (%)	0
Clashscore	4.6

**Table S2.**

Crystallography statistics for PI-ITSN1(WT), dark-state mutant PI-ITSN1(C450M), and PI-ITSN1(WT):Cdc42 complex. \* Values in parentheses are for the highest resolution shell.

	PI-ITSN1 <sub>WT</sub>	PI-ITSN1 <sub>C450M</sub>	PI-ITSN1 <sub>WT:Cdc42</sub>
<b>Data collection</b>			
Space group	<i>P</i> 12 <sub>1</sub> 1	<i>P</i> 12 <sub>1</sub> 1	<i>P</i> 2 <sub>1</sub> 2 <sub>1</sub> 2 <sub>1</sub>
Cell dimensions			
<i>a, b, c</i> (Å)	61.7, 111.2, 88.2	62.1, 111.5, 88.3	112.4, 119.1, 131.1
$\alpha, \beta, \gamma$ (°)	90.0, 90.1, 90.0	90.0, 90.6, 90.0	90.0, 90.0, 90.0
Resolution (Å)	50-2.6 (2.7-2.6)*	50-2.6 (2.7-2.6)*	50-3.3 (3.4-3.3)*
No. unique reflections	35551 (3789)*	36823 (3900)*	27085 (2292)*
$R_{\text{merge}}$	0.059 (0.453)*	0.070 (0.548)*	0.070 (0.524)*
$I/\sigma I$	12.5 (2.6)*	17.9 (3.6)*	23.3 (3.8)*
Completeness (%)	97.0 (97.2)*	99.4 (99.2)*	99.9 (99.9)*
Redundancy	3.4 (3.5)*	6.6 (6.9)*	6.6 (6.3)*
Wilson B (Å <sup>2</sup> )	66.1	63.5	73.2
<b>Refinement</b>			
Molecules per a.u.	2	2	4
Resolution (Å)	47.0-2.6	47.2-2.6	47.4-3.3
No. unique reflections	35516	36785	27076
$R_{\text{work}}/R_{\text{free}}$	0.2515/0.2811	0.2379/0.2846	0.2069/0.2573
No. atoms	7915	7887	10477
Protein	7778	7782	10359
Ligand/ion	62	62	118
Water	75	43	0
<i>B</i> -factors	84.0	77.7	100.8
Protein	84.6	78.0	101.1
Ligand/ion	49.3	52.5	69.5
Water	52.8	50.6	0
R.m.s. deviations			
Bond lengths (Å)	0.002	0.002	0.002
Bond angles (°)	0.547	0.510	0.619
Ramachandran			
favored (%)	96.3	95.5	96.3
outliers (%)	0.2	0.2	0.2
Clashscore	4.7	4.3	5.2

**Table S3.** Insertion sites for all designs. \* represents the switches that were selected for further studies.

Target protein	Species	Target domain	Inserted sequence	Loop	Insertion residue
Src	Mouse	Kinase	LOV2	L1*	Replace G296
Src	Mouse	Kinase	G-LOV2-G	L1*	Replace G296
Src	Mouse	Kinase	GPG-LOV2-GPG	L1*	Replace G296
Src	Mouse	Kinase	GSG-LOV2-GSG	L1*	Replace G296
Rac1	Human	GTPase	SG-LOV2-GSGG	L1*	Insert between G48-K49
Cdc42	Human	GTPase	GSG-LOV2-GSG	L1*	Insert between G47-G48
RhoA	Human	GTPase	LOV2	L1*	Replace G50
RhoA	Human	GTPase	LOV2	L1*	Insert between G50-K51
Vav2	Mouse	DH	LOV2	L1	Insert between L227-S228
Vav2	Mouse	DH	LOV2	L1	Replace L227
Vav2	Mouse	DH	LOV2	L2	Insert between G260-G261
Vav2	Mouse	DH	GSG-LOV2-GSG	L2	Insert between G260-G261
Vav2	Mouse	DH	LOV2	L3	Replace R299
Vav2	Mouse	DH	GSG-LOV2-GSG	L3	Insert between S298-R299
Vav2	Mouse	DH	LOV2	L4*	Insert between A346-D347
Vav2	Mouse	DH	GPG-LOV2-GPG	L4*	Insert between A346-D347
GEF-H1	Human	DH	LOV2	L4*	Insert between G407-I408
GEF-H1	Human	DH	GSG-LOV2-GSG	L4*	Insert between G407-I408
ITSN1	Human	DH	LOV2	L2	Insert between E1308-K1309
ITSN1	Human	DH	GSG-LOV2-GSG	L2*	Insert between E1308-K1309
ITSN1	Human	DH	LOV2	L4	Insert between E1398-N1399
ITSN1	Human	DH	GSG-LOV2-GSG	L4	Insert between E1398-N1399
Vav2	Mouse	CH	LOV2	L1*	Insert between P26-S27
Vav2	Mouse	CH	GSG-LOV2-GSG	L1*	Insert between P26-S27
Vav2	Mouse	CH	LOV2	L2	Insert between L88-R89
Vav2	Mouse	CH	LOV2	L3	Replace D150
Vav2	Mouse	CH	LOV2	L4	Replace R103
Vav2	Mouse	CH	LOV2	L5	Replace S51
Vav2	Mouse	DH	GPG-uniRapR-GPG	L4*	Insert between A346-D347
ITSN1	Human	DH	P-uniRapR-P	L4	Insert between E1398-N1399
Tiam	Human	DH	P-uniRapR-P	L4*	Insert between A1209-E1210
p115	Human	DH	P-uniRapR-P	L4*	Insert between E5801-E581
Asef	Human	DH	P-uniRapR-P	L4*	Insert between P443-Q444

## Captions for Movies

### Movie S1

An SYF cell expressing PI-Src(YF). PI-Src was localized to focal adhesions before, during, and after irradiation. Irradiation led to retraction and a reduced migration rate. Cells were visualized using PI-Src(YF)-mCherry. Blue dot indicates irradiation.

### Movie S2

An SYF cells expressing PI-Src(YF) retracted and showed reduced edge dynamics when treated with 10  $\mu$ M PP2 inhibitor. Cells were visualized using differential interference contrast.

### Movie S3

SYF cells expressing PI-Src(WT). Irradiation caused the PI-Src(WT) to reversibly translocate to focal adhesions. This was accompanied to varying degrees by cell polarization, cell translation, and increased edge dynamics. Blue dot indicates irradiation. Cells were visualized using PI-Src(WT)-mCherry.

### Movie S4

A fibroblast expressing PI-Rac1(Q61L). Irradiation produced reversible cell edge retraction, initially as indentations closely spaced along the edge, and then broader retraction of lamellae. Blue dot indicates irradiation. Cells were visualized using PI-Rac1(Q61L)-mCherry.

### Movie S5

A fibroblast expressing PI-Rac1(WT). Irradiation produced reversible cell edge retraction. Blue dot indicates irradiation. Cells were visualized using PI-Rac1(WT)-mCherry.

### Movie S6

A fibroblast expressing PI-RhoA(Q63L) visualized using Lifeact-mCherry fluorescence. Irradiation produced reversible cell protrusion. Blue dot indicates irradiation.

### Movie S7

A fibroblast expressing PI-Cdc42(Q61L) visualized using Lifeact-mCherry fluorescence. Irradiation produced partially reversible cell retractions and accumulation of actin at the cell periphery. Blue dot indicates irradiation.

### Movie S8

HeLa cells expressing PI-Vav2 shrank in the light, and rapidly recovered in the dark. Blue dot indicates irradiation. White arrows point to regions undergoing retraction. Cells were visualized using Lifeact-mCherry.

### Movie S9

A fibroblast expressing uniRapR-Vav2 produced protrusions upon addition of rapamycin. Cells were visualized using mCherry-uniRapR-Vav2.

### **Movie S10**

Fibroblasts expressing PA-Vav2 rounded when irradiated, and underwent contraction when returned to the dark. Blue dot denotes irradiation. Cells were visualized using mCherry-PA-Vav2.

### **Movie S11**

PA-Vav2 and PI-Rac1 in the same cell. Upon irradiation, area and roundness changed as they did in response to PA-Vav2 alone, but edge dynamics were clearly reduced, unlike response to either PA-Vav2 alone or PI-Rac1 alone. Blue dot denotes irradiation. Cells were visualized using mVenus-PI-Rac1.

## References

1. M. Weitzman, K. M. Hahn, Optogenetic approaches to cell migration and beyond. *Curr. Opin. Cell Biol.* **30**, 112–120 (2014). doi:10.1016/j.ceb.2014.08.004 [Medline](#)
2. L. A. Banaszynski, T. J. Wandless, Conditional control of protein function. *Chem. Biol.* **13**, 11–21 (2006). doi:10.1016/j.chembiol.2005.10.010 [Medline](#)
3. A. Levskaya, O. D. Weiner, W. A. Lim, C. A. Voigt, Spatiotemporal control of cell signalling using a light-switchable protein interaction. *Nature* **461**, 997–1001 (2009). doi:10.1038/nature08446 [Medline](#)
4. M. J. Kennedy, R. M. Hughes, L. A. Peteya, J. W. Schwartz, M. D. Ehlers, C. L. Tucker, Rapid blue-light-mediated induction of protein interactions in living cells. *Nat. Methods* **7**, 973–975 (2010). doi:10.1038/nmeth.1524 [Medline](#)
5. H. Yumerefendi, A. M. Lerner, S. P. Zimmerman, K. Hahn, J. E. Bear, B. D. Strahl, B. Kuhlman, Light-induced nuclear export reveals rapid dynamics of epigenetic modifications. *Nat. Chem. Biol.* **12**, 399–401 (2016). doi:10.1038/nchembio.2068 [Medline](#)
6. D. Niopek, D. Benzinger, J. Roensch, T. Draebing, P. Wehler, R. Eils, B. Di Ventura, Engineering light-inducible nuclear localization signals for precise spatiotemporal control of protein dynamics in living cells. *Nat. Commun.* **5**, 4404 (2014). doi:10.1038/ncomms5404 [Medline](#)
7. Y. I. Wu, D. Frey, O. I. Lungu, A. Jaehrig, I. Schlichting, B. Kuhlman, K. M. Hahn, A genetically encoded photoactivatable Rac controls the motility of living cells. *Nature* **461**, 104–108 (2009). doi:10.1038/nature08241 [Medline](#)
8. X. X. Zhou, H. K. Chung, A. J. Lam, M. Z. Lin, Optical control of protein activity by fluorescent protein domains. *Science* **338**, 810–814 (2012). doi:10.1126/science.1226854 [Medline](#)
9. J. H. Choi, A. H. Laurent, V. J. Hilser, M. Ostermeier, Design of protein switches based on an ensemble model of allostery. *Nat. Commun.* **6**, 6968 (2015). doi:10.1038/ncomms7968 [Medline](#)
10. M. Ostermeier, Designing switchable enzymes. *Curr. Opin. Struct. Biol.* **19**, 442–448 (2009). doi:10.1016/j.sbi.2009.04.007 [Medline](#)
11. J. Lee, M. Natarajan, V. C. Nashine, M. Socolich, T. Vo, W. P. Russ, S. J. Benkovic, R. Ranganathan, Surface sites for engineering allosteric control in proteins. *Science* **322**, 438–442 (2008). doi:10.1126/science.1159052 [Medline](#)
12. A. V. Karginov, F. Ding, P. Kota, N. V. Dokholyan, K. M. Hahn, Engineered allosteric activation of kinases in living cells. *Nat. Biotechnol.* **28**, 743–747 (2010). doi:10.1038/nbt.1639 [Medline](#)
13. O. Dagliyan, D. Shirvanyants, A. V. Karginov, F. Ding, L. Fee, S. N. Chandrasekaran, C. M. Freisinger, G. A. Smolen, A. Huttenlocher, K. M. Hahn, N. V. Dokholyan, Rational design of a ligand-controlled protein conformational switch. *Proc. Natl. Acad. Sci. U.S.A.* **110**, 6800–6804 (2013). doi:10.1073/pnas.1218319110 [Medline](#)

14. B. L. Oakes, D. C. Nadler, A. Flamholz, C. Fellmann, B. T. Staahl, J. A. Doudna, D. F. Savage, Profiling of engineering hotspots identifies an allosteric CRISPR-Cas9 switch. *Nat. Biotechnol.* **34**, 646–651 (2016). doi:10.1038/nbt.3528 [Medline](#)
15. C. L. Tucker, S. Fields, A yeast sensor of ligand binding. *Nat. Biotechnol.* **19**, 1042–1046 (2001). doi:10.1038/nbt1101-1042 [Medline](#)
16. P. H. Chu, D. Tsygankov, M. E. Berginski, O. Dagliyan, S. M. Gomez, T. C. Elston, A. V. Karginov, K. M. Hahn, Engineered kinase activation reveals unique morphodynamic phenotypes and associated trafficking for Src family isoforms. *Proc. Natl. Acad. Sci. U.S.A.* **111**, 12420–12425 (2014). doi:10.1073/pnas.1404487111 [Medline](#)
17. S. M. Harper, L. C. Neil, K. H. Gardner, Structural basis of a phototropin light switch. *Science* **301**, 1541–1544 (2003). doi:10.1126/science.1086810 [Medline](#)
18. A. S. Halavaty, K. Moffat, N- and C-terminal flanking regions modulate light-induced signal transduction in the LOV2 domain of the blue light sensor phototropin 1 from *Avena sativa*. *Biochemistry* **46**, 14001–14009 (2007). doi:10.1021/bi701543e [Medline](#)
19. X. Yao, M. K. Rosen, K. H. Gardner, Estimation of the available free energy in a LOV2-J alpha photoswitch. *Nat. Chem. Biol.* **4**, 491–497 (2008). doi:10.1038/nchembio.99 [Medline](#)
20. A. R. Fersht, L. Serrano, Principles of protein stability derived from protein engineering experiments. *Curr. Opin. Struct. Biol.* **3**, 75–83 (1993). doi:10.1016/0959-440X(93)90205-Y
21. M. P. Playford, M. D. Schaller, The interplay between Src and integrins in normal and tumor biology. *Oncogene* **23**, 7928–7946 (2004). doi:10.1038/sj.onc.1208080 [Medline](#)
22. Y. Zhou, M. Karplus, Interpreting the folding kinetics of helical proteins. *Nature* **401**, 400–403 (1999). doi:10.1038/43937 [Medline](#)
23. F. Ding, D. Tsao, H. Nie, N. V. Dokholyan, Ab initio folding of proteins with all-atom discrete molecular dynamics. *Structure* **16**, 1010–1018 (2008). doi:10.1016/j.str.2008.03.013 [Medline](#)
24. V. J. Fincham, M. C. Frame, The catalytic activity of Src is dispensable for translocation to focal adhesions but controls the turnover of these structures during cell motility. *EMBO J.* **17**, 81–92 (1998). doi:10.1093/emboj/17.1.81 [Medline](#)
25. V. G. Brunton, E. Avizienyte, V. J. Fincham, B. Serrels, C. A. Metcalf 3rd, T. K. Sawyer, M. C. Frame, Identification of Src-specific phosphorylation site on focal adhesion kinase: Dissection of the role of Src SH2 and catalytic functions and their consequences for tumor cell behavior. *Cancer Res.* **65**, 1335–1342 (2005). doi:10.1158/0008-5472.CAN-04-1949 [Medline](#)
26. H. Wang, M. Vilela, A. Winkler, M. Tarnawski, I. Schlichting, H. Yumerefendi, B. Kuhlman, R. Liu, G. Danuser, K. M. Hahn, LOVTRAP: An optogenetic system for photoinduced protein dissociation. *Nat. Methods* **13**, 755–758 (2016). doi:10.1038/nmeth.3926 [Medline](#)

27. M. Machacek, L. Hodgson, C. Welch, H. Elliott, O. Pertz, P. Nalbant, A. Abell, G. L. Johnson, K. M. Hahn, G. Danuser, Coordination of Rho GTPase activities during cell protrusion. *Nature* **461**, 99–103 (2009). doi:10.1038/nature08242 [Medline](#)
28. G. L. Razidlo, B. Schroeder, J. Chen, D. D. Billadeau, M. A. McNiven, Vav1 as a central regulator of invadopodia assembly. *Curr. Biol.* **24**, 86–93 (2014). doi:10.1016/j.cub.2013.11.013 [Medline](#)
29. K. Abe, K. L. Rossman, B. Liu, K. D. Ritola, D. Chiang, S. L. Campbell, K. Burridge, C. J. Der, Vav2 is an activator of Cdc42, Rac1, and RhoA. *J. Biol. Chem.* **275**, 10141–10149 (2000). doi:10.1074/jbc.275.14.10141 [Medline](#)
30. T. Samson, C. Welch, E. Monaghan-Benson, K. M. Hahn, K. Burridge, Endogenous RhoG is rapidly activated after epidermal growth factor stimulation through multiple guanine-nucleotide exchange factors. *Mol. Biol. Cell* **21**, 1629–1642 (2010). doi:10.1091/mbc.E09-09-0809 [Medline](#)
31. M. L. Markwardt, G.-J. Kremers, C. A. Kraft, K. Ray, P. J. C. Cranfill, K. A. Wilson, R. N. Day, R. M. Wachter, M. W. Davidson, M. A. Rizzo, An improved cerulean fluorescent protein with enhanced brightness and reduced reversible photoswitching. *PLOS ONE* **6**, e17896 (2011). doi:10.1371/journal.pone.0017896 [Medline](#)
32. A. W. Nguyen, P. S. Daugherty, Evolutionary optimization of fluorescent proteins for intracellular FRET. *Nat. Biotechnol.* **23**, 355–360 (2005). doi:10.1038/nbt1066 [Medline](#)
33. J. Goedhart, L. van Weeren, M. A. Hink, N. O. E. Vischer, K. Jalink, T. W. J. Gadella Jr., Bright cyan fluorescent protein variants identified by fluorescence lifetime screening. *Nat. Methods* **7**, 137–139 (2010). doi:10.1038/nmeth.1415 [Medline](#)
34. J. H. Kim, S.-R. Lee, L.-H. Li, H.-J. Park, J.-H. Park, K. Y. Lee, M.-K. Kim, B. A. Shin, S.-Y. Choi, High cleavage efficiency of a 2A peptide derived from porcine teschovirus-1 in human cell lines, zebrafish and mice. *PLOS ONE* **6**, e18556 (2011). doi:10.1371/journal.pone.0018556 [Medline](#)
35. W. Kabsch, Integration, scaling, space-group assignment and post-refinement. *Acta Crystallogr. D Biol. Crystallogr.* **66**, 133–144 (2010). doi:10.1107/S0907444909047374 [Medline](#)
36. A. J. McCoy, R. W. Grosse-Kunstleve, P. D. Adams, M. D. Winn, L. C. Storoni, R. J. Read, Phaser crystallographic software. *J. Appl. Crystallogr.* **40**, 658–674 (2007). doi:10.1107/S0021889807021206 [Medline](#)
37. P. Emsley, B. Lohkamp, W. G. Scott, K. Cowtan, Features and development of Coot. *Acta Crystallogr. D Biol. Crystallogr.* **66**, 486–501 (2010). doi:10.1107/S0907444910007493 [Medline](#)
38. P. D. Adams, P. V. Afonine, G. Bunkóczki, V. B. Chen, I. W. Davis, N. Echols, J. J. Headd, L.-W. Hung, G. J. Kapral, R. W. Grosse-Kunstleve, A. J. McCoy, N. W. Moriarty, R. Oeffner, R. J. Read, D. C. Richardson, J. S. Richardson, T. C. Terwilliger, P. H. Zwart, PHENIX: A comprehensive Python-based system for macromolecular structure solution. *Acta Crystallogr. D Biol. Crystallogr.* **66**, 213–221 (2010). doi:10.1107/S0907444909052925 [Medline](#)

39. D. Svergun, Determination of the regularization parameter in indirect-transform methods using perceptual criteria. *J. Appl. Cryst.* **25**, 495–503 (1992). [doi:10.1107/S0021889892001663](https://doi.org/10.1107/S0021889892001663)
40. D. Franke, D. I. Svergun, DAMMIF, a program for rapid ab-initio shape determination in small-angle scattering. *J. Appl. Crystallogr.* **42**, 342–346 (2009). [doi:10.1107/S0021889809000338](https://doi.org/10.1107/S0021889809000338) [Medline](#)
41. V. V. Volkov, D. I. Svergun, Uniqueness of ab initio shape determination in small-angle scattering. *J. Appl. Cryst.* **36**, 860–864 (2003). [doi:10.1107/S0021889803000268](https://doi.org/10.1107/S0021889803000268)
42. D. Svergun, C. Barberato, M. H. J. Koch, CRYSTOL - a program to evaluate Xray solution scattering of biological macromolecules from atomic coordinates. *J. Appl. Cryst.* **28**, 768–773 (1995). [doi:10.1107/S0021889895007047](https://doi.org/10.1107/S0021889895007047)
43. R. Lindner, X. Lou, J. Reinstein, R. L. Shoeman, F. A. Hamprecht, A. Winkler, Hexicon 2: Automated processing of hydrogen-deuterium exchange mass spectrometry data with improved deuteration distribution estimation. *J. Am. Soc. Mass Spectrom.* **25**, 1018–1028 (2014). [doi:10.1007/s13361-014-0850-y](https://doi.org/10.1007/s13361-014-0850-y) [Medline](#)
44. S. D. Slattery, K. M. Hahn, A high-content assay for biosensor validation and for examining stimuli that affect biosensor activity. *Curr. Protoc. Cell Biol.* **65**, 1–31, 31 (2014). [doi:10.1002/0471143030.cb1415s65](https://doi.org/10.1002/0471143030.cb1415s65) [Medline](#)
45. O. Pertz, L. Hodgson, R. L. Klemke, K. M. Hahn, Spatiotemporal dynamics of RhoA activity in migrating cells. *Nature* **440**, 1069–1072 (2006). [doi:10.1038/nature04665](https://doi.org/10.1038/nature04665) [Medline](#)
46. C. C. Liang, A. Y. Park, J. L. Guan, In vitro scratch assay: A convenient and inexpensive method for analysis of cell migration in vitro. *Nat. Protoc.* **2**, 329–333 (2007). [doi:10.1038/nprot.2007.30](https://doi.org/10.1038/nprot.2007.30) [Medline](#)
47. D. Tsygankov, P. H. Chu, H. Chen, T. C. Elston, K. M. Hahn, User-friendly tools for quantifying the dynamics of cellular morphology and intracellular protein clusters. *Methods Cell Biol.* **123**, 409–427 (2014). [doi:10.1016/B978-0-12-420138-5.00022-7](https://doi.org/10.1016/B978-0-12-420138-5.00022-7) [Medline](#)
48. D. Tsygankov, C. G. Bilancia, E. A. Vitriol, K. M. Hahn, M. Peifer, T. C. Elston, CellGeo: A computational platform for the analysis of shape changes in cells with complex geometries. *J. Cell Biol.* **204**, 443–460 (2014). [doi:10.1083/jcb.201306067](https://doi.org/10.1083/jcb.201306067) [Medline](#)
49. D. J. Barry, C. H. Durkin, J. V. Abella, M. Way, Open source software for quantification of cell migration, protrusions, and fluorescence intensities. *J. Cell Biol.* **209**, 163–180 (2015). [doi:10.1083/jcb.201501081](https://doi.org/10.1083/jcb.201501081) [Medline](#)
50. L. Hodgson, P. Nalbant, F. Shen, K. Hahn, Imaging and photobleach correction of Mero-CBD, sensor of endogenous Cdc42 activation. *Methods Enzymol.* **406**, 140–156 (2006). [doi:10.1016/S0076-6879\(06\)06012-5](https://doi.org/10.1016/S0076-6879(06)06012-5) [Medline](#)
51. C. Wu, S. B. Asokan, M. E. Berginski, E. M. Haynes, N. E. Sharpless, J. D. Griffith, S. M. Gomez, J. E. Bear, Arp2/3 is critical for lamellipodia and response to extracellular matrix cues but is dispensable for chemotaxis. *Cell* **148**, 973–987 (2012). [doi:10.1016/j.cell.2011.12.034](https://doi.org/10.1016/j.cell.2011.12.034) [Medline](#)

52. M. E. Berginski, E. A. Vitriol, K. M. Hahn, S. M. Gomez, High-resolution quantification of focal adhesion spatiotemporal dynamics in living cells. *PLOS ONE* **6**, e22025 (2011). doi:10.1371/journal.pone.0022025 [Medline](#)
53. M. Heinig, D. Frishman, STRIDE: A web server for secondary structure assignment from known atomic coordinates of proteins. *Nucleic Acids Res.* **32** (Web Server), W500–W502 (2004). doi:10.1093/nar/gkh429 [Medline](#)
54. R. D. Finn, A. Bateman, J. Clements, P. Coggill, R. Y. Eberhardt, S. R. Eddy, A. Heger, K. Hetherington, L. Holm, J. Mistry, E. L. L. Sonnhammer, J. Tate, M. Punta, Pfam: The protein families database. *Nucleic Acids Res.* **42** (D1), D222–D230 (2014). doi:10.1093/nar/gkt1223 [Medline](#)
55. F. L. Simonetti, E. Teppa, A. Chernomoretz, M. Nielsen, C. Marino Buslje, MISTIC: Mutual information server to infer coevolution. *Nucleic Acids Res.* **41** (W1), W8–W14 (2013). doi:10.1093/nar/gkt427 [Medline](#)
56. J. Yang, R. Yan, A. Roy, D. Xu, J. Poisson, Y. Zhang, The I-TASSER Suite: Protein structure and function prediction. *Nat. Methods* **12**, 7–8 (2015). doi:10.1038/nmeth.3213 [Medline](#)
57. J. Bonet, J. Planas-Iglesias, J. Garcia-Garcia, M. A. Marín-López, N. Fernandez-Fuentes, B. Oliva, ArchDB 2014: Structural classification of loops in proteins. *Nucleic Acids Res.* **42** (D1), D315–D319 (2014). doi:10.1093/nar/gkt1189 [Medline](#)
58. D. Shirvanyants, F. Ding, D. Tsao, S. Ramachandran, N. V. Dokholyan, Discrete molecular dynamics: An efficient and versatile simulation method for fine protein characterization. *J. Phys. Chem. B* **116**, 8375–8382 (2012). doi:10.1021/jp2114576 [Medline](#)
59. S. Ramachandran, P. Kota, F. Ding, N. V. Dokholyan, Automated minimization of steric clashes in protein structures. *Proteins* **79**, 261–270 (2011). doi:10.1002/prot.22879 [Medline](#)
60. S. Sharma, F. Ding, N. V. Dokholyan, Multiscale modeling of nucleosome dynamics. *Biophys. J.* **92**, 1457–1470 (2007). doi:10.1529/biophysj.106.094805 [Medline](#)
61. X. Cai, D. Lietha, D. F. Ceccarelli, A. V. Karginov, Z. Rajfur, K. Jacobson, K. M. Hahn, M. J. Eck, M. D. Schaller, Spatial and temporal regulation of focal adhesion kinase activity in living cells. *Mol. Cell. Biol.* **28**, 201–214 (2008). doi:10.1128/MCB.01324-07 [Medline](#)
62. R. García-Mata, K. Wennerberg, W. T. Arthur, N. K. Noren, S. M. Ellerbroek, K. Burridge, Analysis of activated GAPs and GEFs in cell lysates. *Methods Enzymol.* **406**, 425–437 (2006). doi:10.1016/S0076-6879(06)06031-9 [Medline](#)
63. M. Vendruscolo, Protein dynamics under light control. *Nat. Chem. Biol.* **4**, 449–450 (2008). doi:10.1038/nchembio0808-449 [Medline](#)